FIELD EMISSION BASED DISPLACEMENT SENSING USING A CARBON NANOTUBE ENHANCED ELECTROMECHANICAL PROBE

by

RUDOLPH WILLIAM RESCH

A DISSERTATION

Presented to the Department of Physics
and the Graduate School of the University of Oregon
in partial fulfillment of the requirements
for the degree of
Doctor of Philosophy

June 2020

DISSERTATION APPROVAL PAGE

Student: Rudolph William Resch

Title: Field Emission Based Displacement Sensing Using a Carbon Nanotube Enhanced Electromechanical Probe

This dissertation has been accepted and approved in partial fulfillment of the requirements for the Doctor of Philosophy degree in the Department of Physics by:

Richard Taylor	Chair
Benjamín Alemán	Advisor
Steven van Enk	Core Member
George Nazin	Institutional Representative

and

Kate Mondloch	Interim Vice Provost and Dean of the Graduate School

Original approval signatures are on file with the University of Oregon Graduate School.

Degree awarded June 2020

© 2020 Rudolph William Resch
This work is licensed under a Creative Commons
Attribution-NonCommercial-NoDerivs (United States) License.

DISSERTATION ABSTRACT

Rudolph William Resch

Doctor of Philosophy

Department of Physics

June 2020

Title: Field Emission Based Displacement Sensing Using a Carbon Nanotube Enhanced Electromechanical Probe

The simple measurement of a distance has long powered sensitive scientific instruments. In the case of scanning probe microscopy (SPM), instruments like Scanning Tunneling Microsopes (STM) and Atomic Force Microscopes (AFM) are powered by ultra-sensitive rulers, measuring atomic-scale distances between their probes and the surface. These instruments opened the doors to direct investigation of the nanoscale world. A decade before, however, was a long forgotten instrument known as the Topografiner. Unlike STM and AFM, the Topografiner used an incredibly sensitive long-range ruler based on a field emission current produced by a sharp metal tip. Most importantly, the long range allows for non-contact investigations of topography and surface properties. Unfortunately, the noisy dc field emission techniques used in its operation and the tip-geometry hindered the potential of the technique to reach atomic-scale resolution. We address these issues by using a high-aspect-ratio carbon nanotube as a field emitter and

leverage ac electromechanical coupling to incorporate phase locked loop measurement techniques. These together form a new platform for high precision displacement sensing.

We achieve vertical displacement sensing with sub-atomic resolution at room temperature, with a position sensitivity of $\eta = (7 \pm 4) \cdot 10^2\,\mathrm{fm}/\sqrt{\mathrm{Hz}}$ while the emitter is located at $z \sim 250\,\mathrm{nm}$ from the surface, and $\eta \sim 100\,\mathrm{pm}/\sqrt{\mathrm{Hz}}$ at $z \sim 1\,\mu\mathrm{m}$. This displacement sensitivity approaches that of AFM and STM, with the advantage of a long working distance and large dynamic range. Our electromechanical model shows this improved performance is due to the large aspect ratio and nanometer scale dimensions of the nanotube. The revived topografiner will enable atomic-resolution, high dynamic range SPM imaging, and could also be used to measure and map driven nanomechanical systems or subsurface metallic structures.

This dissertation contains previously unpublished co-authored material.

CURRICULUM VITAE

NAME OF AUTHOR: Rudolph William Resch

GRADUATE AND UNDERGRADUATE SCHOOLS ATTENDED:

University of Oregon, Eugene, OR
Harvey Mudd College, Claremont, CA

DEGREES AWARDED:

Doctor of Philosophy, Physics, University of Oregon 2020
Master of Science, Physics, University of Oregon 2020
Bachelor of Science, Physics, Harvey Mudd College 2009

AREAS OF SPECIAL INTEREST:

Condensed Matter, Nanoscale Systems, Carbon Nanotubes, Low Dimensional Systems, Field Emission, Nanofabrication, Metrology

PROFESSIONAL EXPERIENCE:

Graduate Research Assistant, Alemán Lab, University of Oregon 2014-2020

Graduate Teaching Fellow, University of Oregon 2012-2020

Research Assistant, SLAC National Accelerator Laboratory 2009-2012

PUBLICATIONS:

Resch, R., Zettl, A., & Alemán, B. "Sub-picometer resolution position sensing with a field-emitting carbon nanotube electromechanical resonator." (In Preparation)

P. Scherpelz, R. Resch, D. Berryrieser, T. W. Lynn, "Entanglement-secured single-qubit quantum secret-sharing," *Physical Review A* 84, 032303 (2011)

ACKNOWLEDGEMENTS

Firstly, I would like to thank my advisor, Professor Benjamín Alemán for his continued support and guidance over the course of my dissertation. Thank you for making the gamble when you took me on as your first student. Your knowledge of science and communication has greatly contributed to my development as a physicist.

I would like to thank the members of my committee for their feedback and support from my comprehensive exam all the way to my defense: Richard Taylor, Steven van Enk, and George Nazin.

I would like to thank Professor Ben McMorran, who has been a constant source of advice and assistance over the years.

I would like to thank Professor Stephen Gregory for our late night discussions and worldly counsel.

I would like to thank my colleagues in research: Emily, Kara, David, Andrew, Josh, Brittany, and Rachael. Thank you for your conversations, company, and support. You have all been instrumental in making the Alemán lab what it is today.

I would like to thank the people who keep CAMCOR running, without whom my research could not have been accomplished: Kurt Langworthy, Steve Wiemholt, Fuding Lin, and Bobby Fischer.

I would like to thank the staff of the TSA: John Boosinger, Jeffrey Garman, Clifford Dax, and the late Kris Johnson. The skills I learned and the discussions we had during my time in the machine shop were invaluable for completing my research.

I would like to thank all of the administrative staff in the Physics Department, OMQ, and MSI.

I would like to thank all of my past teachers, professors, and mentors, especially Theresa Lynn, and Eduardo do Couto e Silva.

I would like to thank my colleagues from when I was at SLAC for encouraging my future: Astrid Tomada, Matt Cherry, Jasmine Hasi, Richard Partridge, Paul Brink, Daniel Brandt, and everyone else in the CDMS group.

I would like to thank my family, extended and close for their constant support, especially my parents, Betsy and Michael, my sister Sarah, and my brother Luke.

I would like to thank all the friends I have made here in Eugene, especially the cohort that started this journey with me: Mayra, Jason, Gabriel, and Wes. We all made it.

Finally, I would like to thank my partner, Christina. I would not have made it here without your support, love, and friendship.

To Christina

TABLE OF CONTENTS

Chapter Page

I. INTRODUCTION 1

1.1. Measuring Distances 1
1.2. Rulers 1
1.3. Scanning Probe Microscopy 2
1.4. Topografiner 3
1.5. Alternative Field Emitters 4

II. FIELD EMISSION 7

2.1. Introduction 7
2.2. Fowler Nordheim Equation 8
2.3. Field Enhancement Factor 9
2.4. Geometric Basis of the Field Enhancement Factor 11
2.5. Field Enhancement Near Surfaces 12

III. EXPERIMENTAL SETUP 15

3.1. Vacuum System 15
3.2. Optical Setup 17
3.3. Electronics 18

Chapter Page

3.4. Nanopositioners . . . 19

3.5. SmarAct Stages . . . 23

3.6. Probe Holder . . . 24

3.7. Piezo Calibration . . . 25

IV. PROBE FABRICATION . . . 28

4.1. CNT Sample . . . 28

4.2. Assembly of Probe . . . 29

4.3. Probe Transport . . . 31

4.4. Probe Characterization . . . 32

V. FIELD EMISSION DISPLACEMENT SENSING . . . 35

5.1. DC measurements . . . 35

5.1.1. Modifications to the Fowler-Nordheim Fit . . . 38

5.2. Lock-In Amplification . . . 39

5.3. Verification of Field Emission Transduction . . . 43

5.4. Lock-In Enhanced Topografiner . . . 43

5.5. Amplitude Modulation . . . 46

5.6. Frequency Modulation . . . 48

5.7. Slow Displacement Measurements . . . 52

5.8. Topographic Measurements . . . 55

Chapter Page

VI. THEORY AND SIMULATIONS 59

6.1. Derivation of Capacitive Spring Constant 59

6.2. Capacitance Simulations 60

6.3. Bare AFM Tip Measurements 65

6.4. Broadening in Topographic Scans 66

6.4.1. Lateral Deflection 69

VII. CONCLUDING REMARKS 73

7.1. Summary 73

7.2. Future Work 74

APPENDICES

A. FABRICATION DETAILS 75

A.1. AFM/CNT device fabrication: 75

A.2. On-chip device fabrication: 75

A.3. Fabrication Techniques 76

A.3.1. Carbon Nanotube Solution 76

A.3.2. Drop casting carbon nanotubes 76

A.3.3. Spin casting carbon nanotubes 76

Chapter Page

B. CARE AND FEEDING OF VACUUM CHAMBER 77

B.1. General Notes 77

B.1.1. Base Pressure 77

B.1.2. Material Considerations 77

B.2. Components 78

B.2.1. Chamber 78

B.2.2. Heating Elements 79

B.2.3. Pumps 80

B.2.4. Chamber Interior 81

B.3. Labview Control/Monitor 82

B.3.1. Future Improvements 84

B.4. Venting Procedure 84

B.5. Pump Down Procedure 85

REFERENCES CITED 86

LIST OF FIGURES

Figure Page

1.1. Diagram of Topografiner . . . 3

1.2. Schematic of a carbon nanotube . . . 5

2.1. Position dependence of field emission . . . 8

2.2. Compression of equipotential lines due to a protrusion on a surface . . . 10

2.3. Simulation results for enhancement factor (γ) . . . 13

3.1. Picture of vacuum system . . . 16

3.2. Diagram of optical setup . . . 17

3.3. Diagram of electronics setup . . . 18

3.4. Picture of Micronix nanopositioner stage . . . 20

3.5. Calibration for nanopositioner movement . . . 21

3.6. Platform for nanopositioner stages . . . 22

3.7. Picture of Smaract nanopositioner stage . . . 23

3.8. Image of probe holder and PCB design . . . 25

3.9. Orientation of probe holder for CNT attachment and scanning . . . 26

3.10. Calibration of piezo for slow drive measurements . . . 27

4.1. Assembly steps for a CNT probe . . . 29

4.2. Finished field emission probe . . . 30

4.3. Calibration of probe oscillation amplitude . . . 31

4.4. IV curves before and after annealing probe . . . 33

4.5. Example of Fowler-Nordheim Curve for field emission probe . . . 34

Figure Page

5.1. Results for displacement sensing using dc current. 36

5.2. Field emission current as a function of time 37

5.3. Example of resonance curve measured using field emission 40

5.4. Thermal resonance peak measured using field emission 41

5.5. Verification of field emission transduction 42

5.6. Spectrogram of resonance curves and peak R values 44

5.7. Displacement sensitivity measured using peak R and AM techniques . . 45

5.8. Illustration of resonance sensing technique 46

5.9. Gap dependence of resonator frequency 48

5.10. Allan deviation for FM displacement sensitivity measurement 50

5.11. Displacement sensitivity using FM technique 51

5.12. Resonance curve before AM slow displacement 52

5.13. Slow displacement measurement using AM technique 54

5.14. Slow displacement measurement using FM technique 55

5.15. Topographic measurement of reference bars on a surface 56

5.16. Cross section of reference bar measured by AFM 58

6.1. Geometry and mesh for full capacitance simulation 61

6.2. Capacitance of carbon nanotube from finite element simulation 62

6.3. Resonator frequency compared with theoretical model 63

6.4. Frequency of bare AFM probe with model 65

6.5. Simulated topographic scan of rectangular bar 67

6.6. Simulated topographic scan of trapezoidal bar 68

6.7. Spread of electric field lines between probe and anode 68

6.8. Geometry and mesh for electromechanical simulations 69

Figure Page

6.9. Simulated electrostatic bending of 5 µm CNT 70

6.10. Simulated electrostatic bending of 1 µm CNT 71

B.1. Picture of vacuum system 78

B.2. Interior of vacuum chamber 81

B.3. Labview VI for Vacuum Control 83

LIST OF TABLES

Table Page

5.1. Frequency to height conversions for topographic scans 57

6.1. Geometric effect of tube, tip, and cantilever on frequency shift 64

CHAPTER I

INTRODUCTION

1.1. Measuring Distances

Since the dawn of humanity, we have wanted to measure distances, often because we are motivated by a question. We can ask "How far away are the stars?" or "What is the size of an atom?" In order to answer these questions, we need tools, or instruments to make measurements. We can use telescopes to find the distance to stars using parallax. More modern instruments, like LIGO, can reach even further, measuring sources of gravitational waves billions of light-years away. On the other end of the size spectrum, scanning probe microscopy (SPM) can be used to measure the size and position of atoms and molecules at the atomic scale. Underlying all of these instruments is some method of measuring distance, or in other words, a ruler.

1.2. Rulers

Some of our most important scientific measurements have been accomplished with simple rulers. In 1927, Albert Michelson made one of the first modern measurements of the speed of light by recording the transit time for flashes of light between two mountains in southern California[1]. This measurement required an extremely advanced survey to map the distance between the two peaks with an accuracy of 1 part in 1 000 000, which was accomplished using 50 m long measuring tapes constructed of invar[2].

Originally predicted in 1916 by Albert Einstein [3], gravitational waves were directly measured for the first time by LIGO in 2015 [4]. These waves are measured

by observing motion in a test mass with amplitudes as small as 10^{-18} m. To do this, LIGO leverages the interference of light waves as a ruler, using an interferometer with arms that are 4 km in length.

1.3. Scanning Probe Microscopy

As a field, scanning probe microscopy (SPM) has enabled incredibly sensitive studies of surface properties and opened the doors to direct investigation of the nanoscale world. The rulers underlying each SPM platform form a feedback system to both control and measure the distance between the probe tip and the surface. The most well known examples of SPM are Scanning Tunneling Microscopy (STM) and Atomic Force Microscopy (AFM).

STM was developed in 1981 by Gerd Binnig and Heinrich Rohrer at the IBM Research Laboratory in Switzerland [5]. The ruler for this technique was realized by using a quantum tunneling current that flows from sharp tip directly into a nearby surface. The tunneling current was exponentially sensitive to distances on the order of a few nanometers away from the surface [6] allowing for extremely fine control of the spacing. Unfortunately, it also means that STM has to be an incredibly short distance from the surface. This sensitivity enabled the first real space, direct images of the atomic lattice in silicon [7]. Due to the impact of the STM on investigations of surface science, Binnig and Rohrer shared part of the Nobel Prize in 1986.

In the same year as the Nobel Prize, Binnig, Quate, and Gerber published on the next great SPM technique, the AFM [8]. This technique relied on short range, atomic scale forces between a sharp tip and a surface to induce motion in a cantilever. By measuring this motion, you could then obtain information about the surface in question. Like STM, the range of these forces means the AFM has to

operate very close to the surface. Initially, the motion was measured using an STM, but soon evolved to use other techniques such as interferometry [9] and optical beam deflection [10].

However, there is another, long forgotten technique that is arguably the first modern scanning probe microscope.

1.4. Topografiner

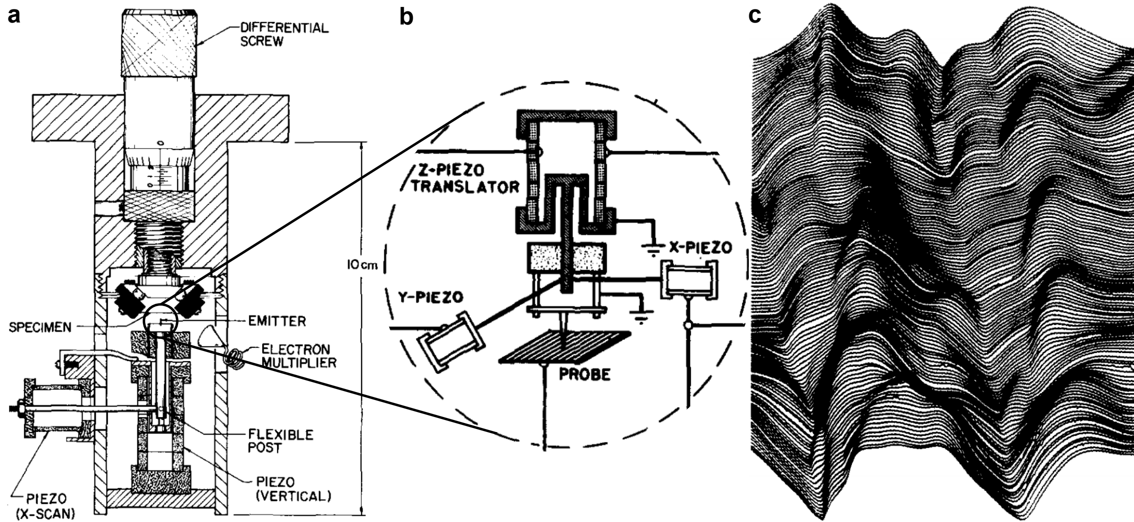

FIGURE 1.1. Diagram of Topografiner. (a) Positioning mechanisms for the Topografiner. (b) Zoom of the XYZ system for scanning across specimens. (c) Topographic scan from the Topografiner of a damaged part of a 180 line/mm diffraction grating. [11]

Developed by Russell Young, ten years before the STM, the Topografiner [11] used a field emission current as its ruler to measure the distance between a metal tip and a surface. This distance measuring technique was explored earlier by Young with what he called the Ultramicrometer [12]. In field emission [13], electrons quantum tunnel through the potential barrier of the probe into free space, where they then propagate to the sample surface. The rate of emission is governed by the local electric

field at the metal tip, which is incredibly sensitive to the tip-surface distance even at several microns. This means the Topografiner is capable of very long range operation compared to the other SPM techniques, allowing the instrument to operate without contacting the surface directly and greatly reducing the probability that the tip crashes into the sample. One obvious advantage of this would be a possible increase in the speed at which the tip could be scanned across as a surface. Another exciting possibility would be using the long range to probe below the surface of a material.

Unfortunately, the Topografiner ultimately failed to achieve long range imaging or sensitive displacement measurements. These shortcomings were caused primarily by the emitter. At the time, emitters were limited by the available materials, and were mostly made of sharpened metal wires. Due to the large radius of curvature of these emitters ($\sim$100 nm), small tip-surface distances of order 10 nm were required to reach the fields required for field emission, thus preventing truly long working distances. This also led to poor lateral resolution, estimated to be $\sim$400 nm by Young. They also noted that the tips would often get rounded off, and theorized this was due to electrical discharge from the ion pumps during pumpdown. Young notes at the end of the publication: "The search continues for an emitter which remains sharp and is less sensitive to ambient gas." This hints at a potential path forward to solve this problem.

1.5. Alternative Field Emitters

Much like a tall metal pole will serve to concentrate lightning strikes, electric fields are enhanced by sharp objects. This means that the use of a high aspect ratio field emitter could make it easier to reach the fields required for emission, and therefore increase the range. With the emergence of nanomaterials, there are many

options available that could be used to replace the emitter in the topografiner. These include nanowires [14], edges of 2D materials [15], FIB sculpted tips [16, 17], and carbon nanotubes [18, 19].

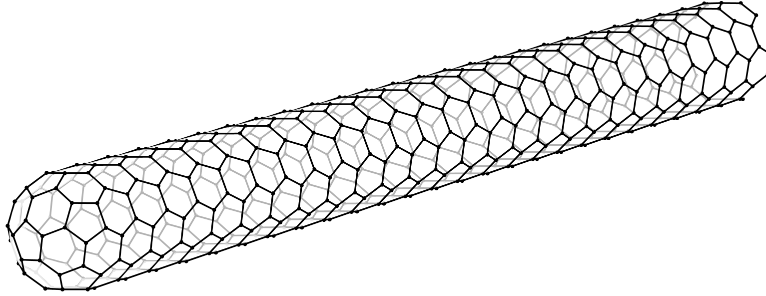

FIGURE 1.2. Schematic of a carbon nanotube. Carbon nanotubes are nanoscale tubes made with the same hexagonal structure as graphene.

Carbon nanotubes [20] (CNTs) are a particularly attractive candidate due to their ultra high aspect ratios (sharpness). They can have radii down to 1 nm and lengths of several microns. CNTs also exhibit unparalleled thermal [21], electrical [22, 23], and mechanical properties [24, 25]. As field emitters, these nanotubes have been able to produce large emission currents ($\sim$100 µA) at relatively low bias ($<$100 V) while located a large distance from the anode ($\sim$10 µm). Additionally, when combined with noise filtering, these emitters have been used to measure nanomechanical motion with nanometer-scale resolution. In one case, Jensen *et al.* used the nanomechanical motion of a field-emitting carbon nanotube as the basis for a nanoscale radio [26]. In another experiment, they were able to use a vibrating nanotube as a nanomechanical sensor, with the mass sensitivity better than a single gold atom using a field emission readout [27].

In this dissertation, I hypothesize that high aspect ratio carbon nanotubes can be used as the basis of a new, high precision displacement measurement technique

based on field emission. In Chapter II, I discuss the basic physics of field emission. In Chapter III, I outline the experimental setup used to test this hypothesis. In Chapter IV, I discuss the fabrication of the carbon nanotube probes. In Chapter V, I measure the displacement sensitivity of these probes, along with improvements using noise filtering from lock-in detection and electromechanical resonance sensing. In Chapter VI, I determine the theory behind the displacement measurements.

CHAPTER II

FIELD EMISSION

The displacement sensing technique used by the original Topografiner was based on a field emission current, where a large electric field assists electrons in tunneling out of a material. In order to understand this displacement sensing technique, we need to understand the basic physics of field emission. In this chapter, I discuss the Fowler-Nordheim equation, which describes the behavior of a field emission current, then I discuss how high aspect ratio structures enhance the process of field emission. From this, there is promise that high aspect ratio field emitters, like carbon nanotubes, will improve the signal to noise ratio in displacement sensing.

2.1. Introduction

Field emission is one of a class of processes whereby electrons are emitted from a material. This class includes thermal emission, field emission, photoemission, and secondary emission. Most of these describe situations where electrons are given enough energy to jump over the potential barrier between the material and outside world. In field emission however, the electrons can quantum mechanically tunnel through this potential barrier. In depth derivations concerning the rate of this tunneling can be found in Jensen [28], Gomer [29], and Ducastelle [30].

2.2. Fowler Nordheim Equation

The equation that governs the behavior of field emission is known as the Fowler-Nordheim equation.

$$J(F) = \frac{q^3}{16\pi^2\hbar\phi t(y)^2} F^2 \exp\left(-\frac{4\sqrt{2m\phi^3}}{3\hbar q} v(y)\frac{1}{F}\right) \tag{2.1}$$

This describes how the field emission current density, J, depends on the applied field, F, at the surface of the emitter. With numerical values[30], this becomes

$$J(F) = \frac{1.42 \cdot 10^{-6}}{\phi} F^2 \exp\left(\frac{10.4}{\sqrt{\phi}}\right) \exp\left(-\frac{6.56 \cdot 10^9 \phi^{3/2}}{F}\right) \tag{2.2}$$

for ϕ measured in eV.

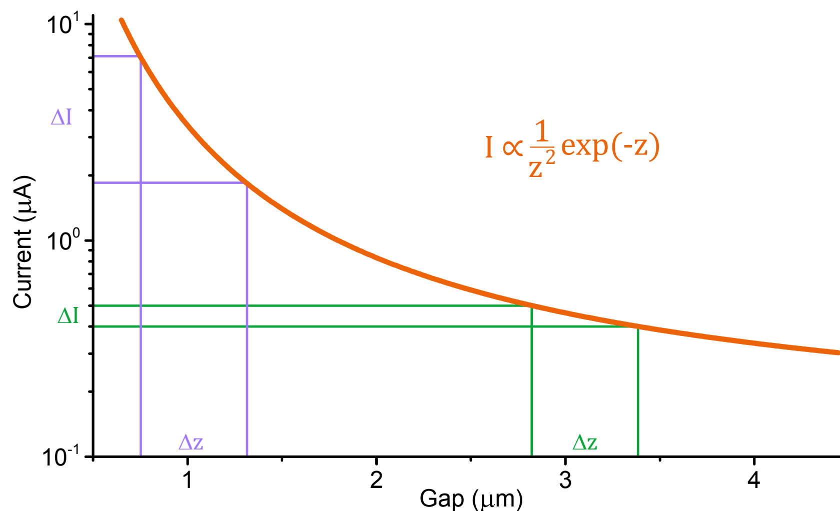

FIGURE 2.1. The field emission current has an exponential dependence on the position of the emitter. If the electric field, $F \propto 1/z$, then the current, $I \propto \exp(-z)/z^2$, as shown by the orange curve. This works as a position or displacement sensor by converting a change in position, Δz, into a measurable signal in the form of ΔI. Field emission has an exponentially increasing signal that depends on position. If we say the green Δz produces one unit of signal (green δI), then for the same Δz at a closer position (purple), the corresponding signal would be over 50 units.

In order to use this as a way to measure distances, we need to look at the the general behavior of the Fowler Nordheim equation. If we take the electric field to go as the inverse of distance, $F \propto 1/z$, then the field emission current will go as $I \propto \exp(-z)/z^2$, exponentially increasing as z gets smaller. This is shown by the orange curve in Figure 2.1. Using that curve, we can see that for some change in position, Δz, there will be a corresponding change in current, ΔI. That change in current would then be a measurable signal. One exciting aspect of the field emission process is that as the position decreases, the same Δz will produce a much larger ΔI, as shown when you compare the green and purple curves. Since this is a logarithmic scale, if we label the green ΔI as one unit of signal, the purple ΔI would be over 50 units for the same distance moved Δz.

2.3. Field Enhancement Factor

The field emission current depends on the electric field at the emission surface, but in order to understand this better, we need to define this field. For a configuration like the parallel plate capacitor, this would be:

$$F_D = \frac{V_0}{D} \tag{2.3}$$

where V_0 is the bias between the two plates and D is the distance between them. Typical fields required for field emission are on the order of $F = 10^9$ V/m. In order to reach this field with a reasonable separation, say $D = 100$ µm apart, the plates would have to be biased at $V_0 = 100$ kV. Fortunately, the presence of any protrusion on the surface (a hemisphere, a cone, a cylinder) will have a tendency to enhance the local electric field on that object.

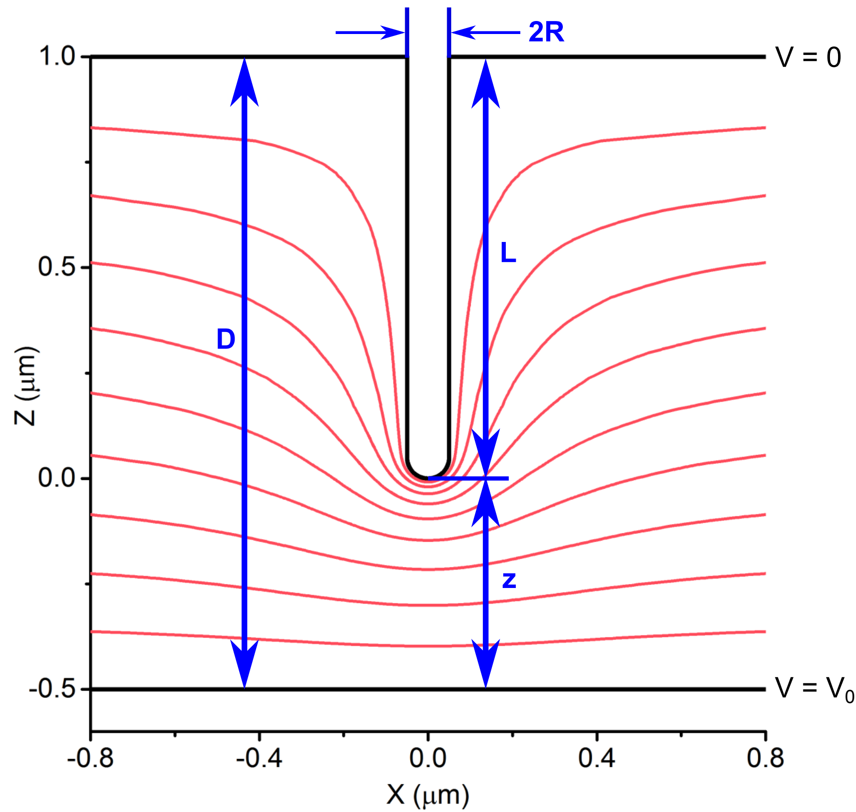

FIGURE 2.2. Compression of equipotential lines due to a protrusion on a surface. The equipotential lines between two parallel plates should be evenly spaced across the entire distance, resulting in a constant electric field. Since these lines cannot cross each other, the presence of a protrusion forces them to compress. Even if they were evenly spaced between the tip of the protrusion and the opposite plate, the electric field in that region would be enhanced. However, the lines closest to the tip of the protrusion are significantly compressed, leading to a very large enhancement of the electric field.

One way to understand this is by looking at the equipotential lines between two plates. If the plates were perfectly flat, the equipotential lines would be evenly spaced from $V\!=\!0$ to $V\!=\!V_0$. However, when these lines encounter a protrusion, as shown in Figure 2.2, they are forced to compress. Where the lines are compressed, the potential changes by a larger amount, over a smaller distance, so $F\!=\partial V/\partial z$ is enhanced. This is especially true near the tip of a sharp protrusion.

We can define a field enhancement factor:

$$\gamma = \frac{F_L}{V_0/z} \tag{2.4}$$

where the local field at the tip of the protrusion, F_L, is compared to the macroscopic field as measured from the tip, F_z=V_0/z. As defined here, $\gamma \to 1$ for $z \ll R$, where the tip of the emitter and the anode would behave like a parallel plate capacitor.

2.4. Geometric Basis of the Field Enhancement Factor

We now want to know how the geometry of the emitter affects the field enhancement factor. The simplest model that can be solved exactly is the case where the emitter is a hemisphere located on a plane. For this situation, it turns out that γ=3. If instead, we place the hemisphere on a post, we find γ=$2 + L/R$[31], where L is the distance from the plane to the top of the hemisphere, and R is the radius of the hemisphere. In the limiting case of L=R we recover the result of the hemisphere. Unfortunately, this tends to drastically overestimate the enhancement for high aspect ratio emitters. Using simulations, Edgcombe and Valdrè [32] came up with a analytic model using D=100 µm and R=10 nm:

$$\gamma = 1.2\left(2.15 + \frac{L}{R}\right)^{0.9} \tag{2.5}$$

which can be approximated as γ=$0.7L/R$ for $30 \leq (L/R) \leq 2000$. They only simulated up to an aspect ratio of 3000, when L=$0.3D$, so still relatively far away from the anode.

Because field emission depends strongly on the aspect ratio of the emitter, carbon nanotubes are a particularly exciting option as field emitters. Carbon

nanotubes, as well as other nanomaterials, can easily reach aspect ratios of 10^4 or more, which means their enhancement factor is on that same order. With this level of enhancement, we can calculate the theoretical required bias for the aforementioned case of the parallel plates for a nanotube with R=10 nm and L=10 µm. Using Equation 2.5, the field would be enhanced by γ=600 using this nanotube. The results of this are astounding. For a typical required field of $4 \cdot 10^9$ V/m, instead of a bias of 100 kV at a distance of 25 µm, as you would need for a set of parallel plates, you could instead use a bias of only 167 V. Alternatively, using the original bias you could theoretically generate a field emission current at a distance of 15 mm! Here we see the huge advantage to using a high aspect ratio emitter, the ability to work with field emission at greatly extended distances compared to those used for the Topografiner. However, as I said before, this enhancement factor should approach 1 for small z, so we need to take this into account.

2.5. Field Enhancement Near Surfaces

In order to understand the enhancement factor near a surface (in a scanning probe configuration for instance), we need to consider the case where $z < L$. Using a model with floating sphere and image charges, Miller [33] took this into account to find:

$$\gamma = \gamma_\infty \frac{z}{z + L} + 1 \tag{2.6}$$

where γ_∞ is the enhancement for large z. The 1 is a modification by Hii *et al.* [34] so that $\gamma(0)$=1. The phenomenon of the enhancement factor plateauing to γ_∞ only occurs for a protrusion between two parallel plates.

To demonstrate this, we performed two simulations for a R=5 nm, L=1 µm nanotube at the end of a 15 µm cone, as would be the case for our probes, discussed

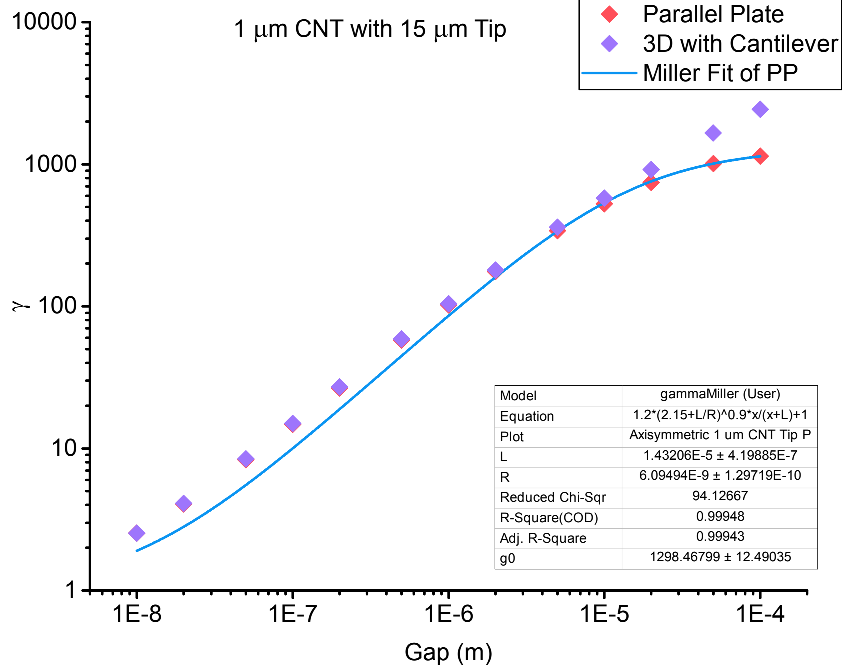

FIGURE 2.3. Simulation of field enhancement factor. 3D model with cantilever vs axisymmetric parallel plate model. For this simulation, we modeled a 1 µm long CNT with a radius of 5 nm at the end of a 15 µm tall cone and found the electric field at the tip of the nanotube. For both the 3D and the axisymmetric model, we found the enhancement factor approaches 1 as the gap approaches 0. For the parallel plate model, the plates were 200 µm in radius, and we found the far field enhancement factor approached $\gamma \sim 1300$. Using a fit to Equation 2.6, the effective length of the CNT and cone was 14.3 µm and the effective radius was 6.1 nm. For the 3D model, the enhancement factor did not plateau during the parameter range we were exploring. The two simulations only diverged for gaps larger than 10 µm.

in future chapters. In one simulation, the nanotube and cone were placed between two parallel plates using an axisymmetric model. In the other simulation, the nanotube and cone were placed at the end of a cantilever using a fully 3D model. The local electric field at the tip of the nanotube is measured and the enhancement factor is calculated using Equation 2.4 for varying values of z. The results are shown in Figure 2.3. Here, we see γ approaches 1 in both models for small z but only for the parallel plate model does γ start to level off at large z. We can also see that the enhancement factors in both simulations match well up to a gap of $z \sim 10\,\mu\text{m}$, where

they differ by $\sim$10%. By fitting the parallel plate simulation with Equation 2.6 and applying Equation 2.5 for γ_∞, we see that the nanotube and cone combined have an effective length of L=14 µm and an effective radius of R=6 nm resulting in $\gamma_\infty \sim 1300$. These simulations show that the enhancement factor is decreased to order 100 for $z\sim$1 µm, which is less than the far field, but still respectable. This value is close to the enhancement factors we measured with our probes.

CHAPTER III

EXPERIMENTAL SETUP

In order to use field emission to measure displacements, we need to control the position of a field emitting nanotube with nanometer scale precision while in a high vacuum environment. In this chapter, I describe the nanopositioner platform that I built, setup, and calibrated for positioning our nanotube probes, and the vacuum system used in the experiments. I also detail the light microscope used for coarse positioning of the probe, and the electronics used to control the apparatus and measure the nanotube field emission.

3.1. Vacuum System

All measurements for these experiments need to be performed in an ultra high vacuum (UHV) environment, typically defined as $< 10^{-9}$ mbar, due to several factors. During the process of field emission, a carbon nanotube can heat up to well in excess of 1000 °C [35]. In an atmospheric environment, this would cause the emitter to oxidize and be destroyed. Another factor is the high electric fields (10^9 V/m) involved with the process of field emission. At these fields, the air near the emitter would undergo dielectric breakdown, which occurs at only 10^6 V/m. Additionally, the process of field emission is incredibly sensitive to the local environment of the emitter. Any contaminants (ions, molecules, etc.) landing on the emitter can drastically change the geometry, and therefore the field strength due to the field enhancement factor.

The vacuum chamber for these experiments, shown in Figure 3.1, has a volume of ∼60 L. On the exterior walls are several feedthroughs for electronics and viewports

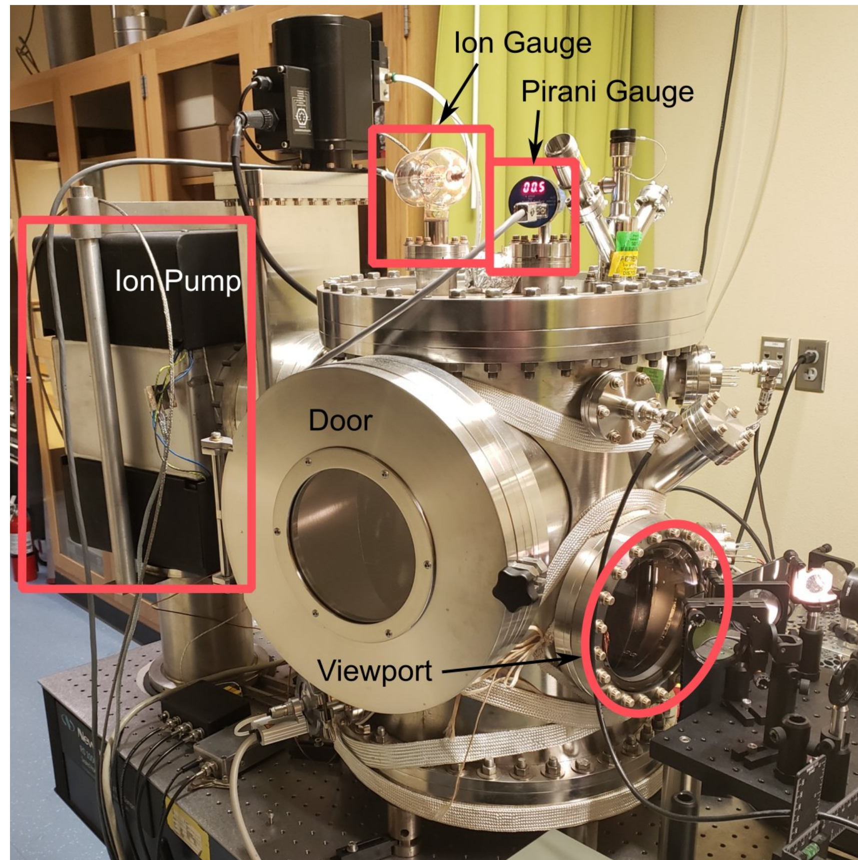

FIGURE 3.1. Vacuum System. The measurements for these experiments have to be done in a vacuum environment. The door for sample exchanges is on the near side. The viewport for optical measurements is on the right. The two vacuum gauges are located on top of the chamber. The turbopump is not pictured, but is on the back side of the chamber. The ion pump is located on the left.

for optical access into the chamber. The chamber is first evacuated by a turbopump, which reduces the pressure to $\sim 10^{-7}$ mbar. After this, an ion pump is used to reach the base pressure of $\sim 10^{-8}$ mbar. Although this is not the ideal UHV pressure, it works well enough for the purposes of these experiments. The pressure is limited by the need to easily exchange samples and probes inside the chamber, requiring a loading door with an elastomer seal. Further details about the vacuum system can be found in Appendix B.

3.2. Optical Setup

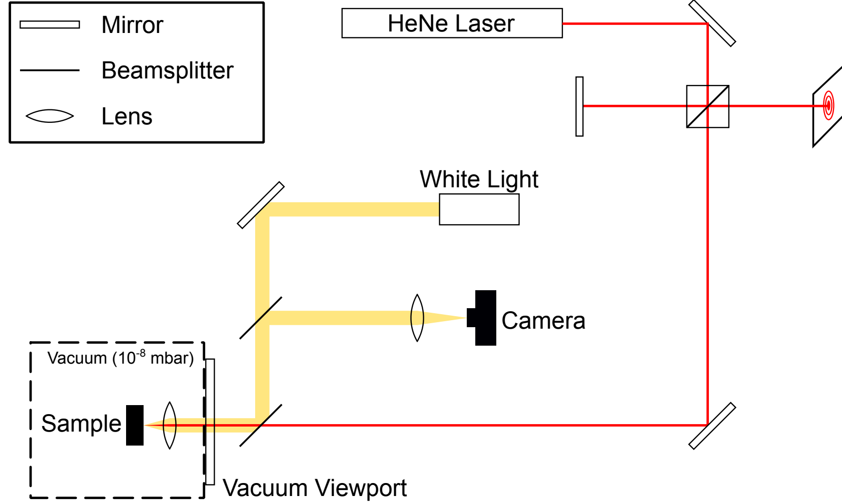

FIGURE 3.2. Diagram of optical setup. The optical setup was composed of two parts, an optical microscope and an interferometer. The objective lens was placed inside the vacuum chamber, near the sample. The optical microscope provided coarse positioning of the probe relative to the sample and anode. The interferometer was used to measure the resonance properties of the AFM cantilevers. The laser itself was also used to align the pitch of the sample using the back reflection.

In order to view the sample inside the vacuum chamber and to position the probe, we built a simple tabletop optical microscope. The objective for the microscope was an f=20.1 mm, 25 mm diameter aspheric lens with NA=0.6. The original design used an aspheric with a much higher NA of 0.8 in order to collect more light. Unfortunately, it had to be replaced due to changes in the geometry of the experimental setup which required a longer working distance. The objective lens was located inside of the vacuum chamber. The simple aspheric lens was used due to vacuum compatible microscope objectives being prohibitively expensive. The other option would have been to place the objective outside of the chamber. The downside to this is that the viewport window was 9 mm thick, which would have required an super long working distance objective (also prohibitively expensive) and would have

introduced a great deal of chromatic aberration. The other element of the optical setup was a HeNe interferometer. This was used to measure the resonance frequency of the AFM cantilevers under vacuum. The laser was also used for alignment of samples by looking at the back reflection. By tilting the sample so the back reflection is co-linear with the incoming beam, the sample is nominally flat, allowing the probe to stay at a constant distance as it scans across the surface.

3.3. Electronics

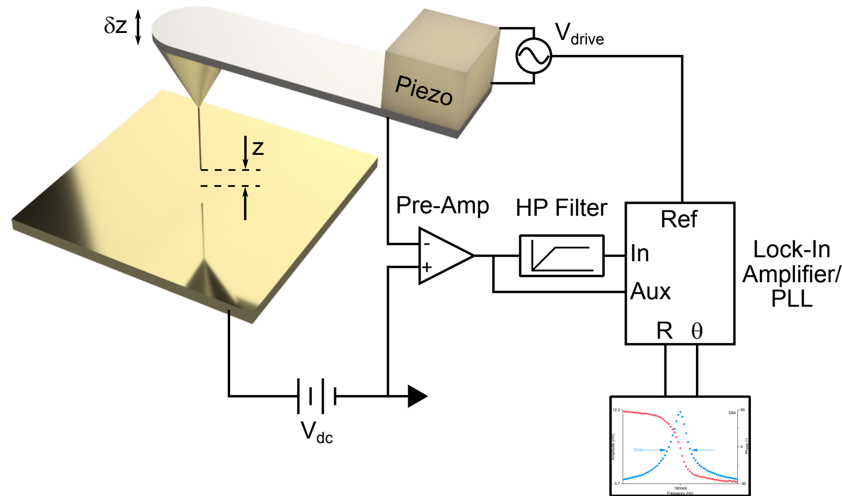

FIGURE 3.3. Diagram of electronics setup. When the probe is positioned a distance z from the anode, a dc bias V_{dc} is used to drive the field emission current. This dc bias is supplied by a Keithley 2450 Source Measure Unit (SMU). The current is amplified and converted into a voltage using a low noise current preamplifier (SRS SR570). This signal is split into two parts to measure the high frequency and dc components separately. The high frequency is measured by a lock-in amplifier (Zurich Instruments MFLI). The dc component is measured by an auxiliary input on the MFLI. The lock-in amplifier provides a reference signal that drives a piezo, causing the probe to oscillate with an amplitude δz. The lock-in amplifier has a built in phase locked loop (PLL) to control the frequency of the reference signal and drive the probe on resonance. The lock-in amplifier outputs a phase and amplitude of the measured oscillations in the field emission current due to the physical vibrations of the probe.

There are three main pieces of electronics used for the experiment. The first is a Source Measure Unit (SMU) (Keithley 2450). This was used to provide the dc bias (V_{dc}) and measure the dc field emission current (I_{dc}). The next is a low noise current preamplifier (Stanford Research Systems SR570). The current signal from a probe is sent to the preamp and converted into a voltage. The output of the current preamplifier was split in two. The first part is sent to the signal input of the lock-in amplifier (Zurich Instruments MFLI) to transduce the oscillations in the field emission current. There is a 10 kHz high pass filter in-line with this signal to block the dc component. The second part was sent to a slower, auxiliary input to measure the dc component. This means the dc component can be time correlated with the lock-in signal. The reference output from the lock-in drives oscillations in the AFM cantilever using the piezo.

3.4. Nanopositioners

The nanopositioners used for the majority of the experiment were open-loop PPS-20 stages from Micronix. These stages have a travel range of 12 mm and a nominal resolution of 1 nm. The combination of large travel range and high resolution is accomplished by the piezo drives undergoing a stick-slip motion. These nanopositioners were chosen because they were relatively inexpensive ($2700 for positioner and controller) for vacuum compatible stages with the aforementioned specifications.

Because the stages are open loop, we do not have a absolute measure on the position of the probe relative to the sample/anode. However, we were able to make careful measurements of the stage movement in an SEM in order to calibrate their step size. An example of one of these calibrations is shown in Figure 3.5. In the

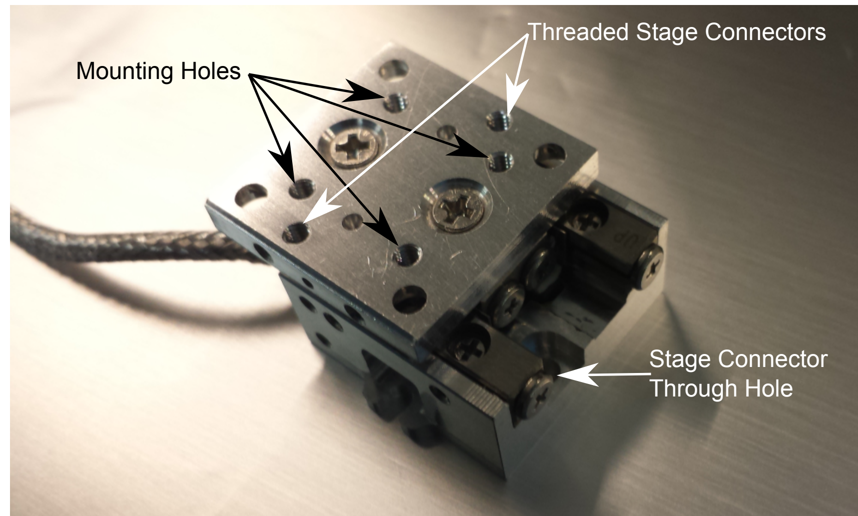

FIGURE 3.4. Single Micronix PPS-20 nanopositioner stage. These stages are 20 mm by 20 mm and 13 mm tall. The upper plate is the moving carriage for the stage which has a movement range of 12 mm. There are four threaded holes on the plate for mounting and are spaced in a 10 mm square pattern. There are also two offset threaded holes for connecting two stages in a stacked XY configuration. The corresponding through holes are on the bottom portion of the stage.

picture, you see a series of "10" nm steps taken by the stage. In this case, the stage was moving in the direction that would decrease the gap between the probe and anode. Approximately every 50 of these steps, the stages will slip as the piezo retracts or extends to start a new series of steps. There are two categories of movement which need to be analyzed. The simplest is when the stages are constantly moving, taking a step every few seconds. The calibration for this movement is shown in Figure 3.5b. Here, step 1 is the first step after the stage slipped, moving it in the direction opposite of the intended motion. The first 15 steps or so are smaller than average in both directions. When increasing the gap, the net distance the stage travels from slip to slip is (650 ± 20) nm. This corresponds to a full movement of the piezo of $\sim$900 nm and a slip of $\sim$250 nm. When decreasing the gap, the net distance is (740 ± 18) nm, or full movement $\sim$825 nm and a slip of $\sim$85 nm. Immediately following a slip, the stage tends to take a very small step, sometimes as low as half an average step.

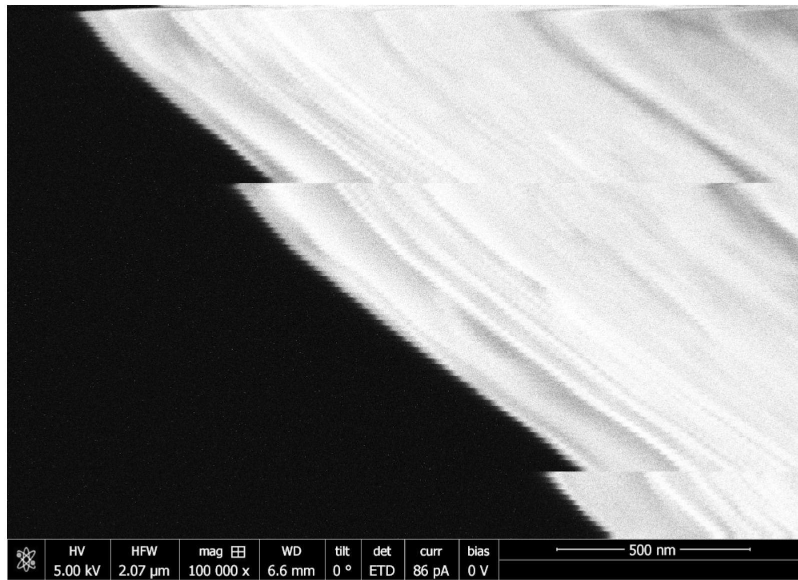

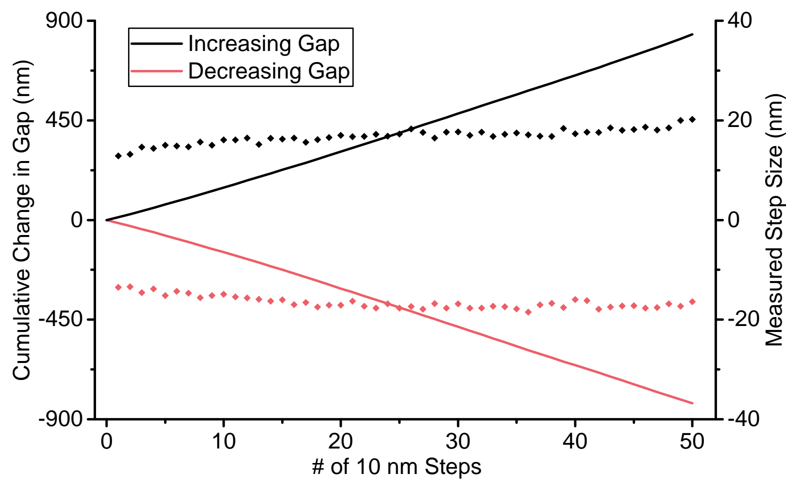

FIGURE 3.5. Calibration for nanopositioner movement. (a) An SEM image of the stage taking steps during a very slow image scan from the top to the bottom. During the scan, the stage was moving to the right. The larger jumps to the left show the stage undergoing the slip part of the stick-slip motion. (b) Data extracted from several SEM images like in part (a). The black points show the measured step size for each "10" nm step taken by the stage when the gap between the probe and anode was increasing. The red points show the same for a decreasing gap. Step number 1 is the first step after the stage slipped. For both directions of motion, the first 15 steps are smaller on average. The stage can take approximately 50 steps before the piezo drive needs to slip again. The black line shows the cumulative distance moved by the stage in the increasing direction. The red line is the cumulative distance for the decreasing direction.

The other category of movement is when there is a long time between steps. This mostly occurs when a resonance curve is taken at each position. During these measurements, there could be a period of minutes between steps, especially if the current is unstable. In this case, the increasing gap step is (13.9 ± 1.8) nm and the decreasing gap step is (13.6 ± 1.6) nm. This was noticed when taking high magnification measurements of the steps and there was a delay between each image in a series of slow scans. The first step of each scan was measurably shorter than the rest on average.

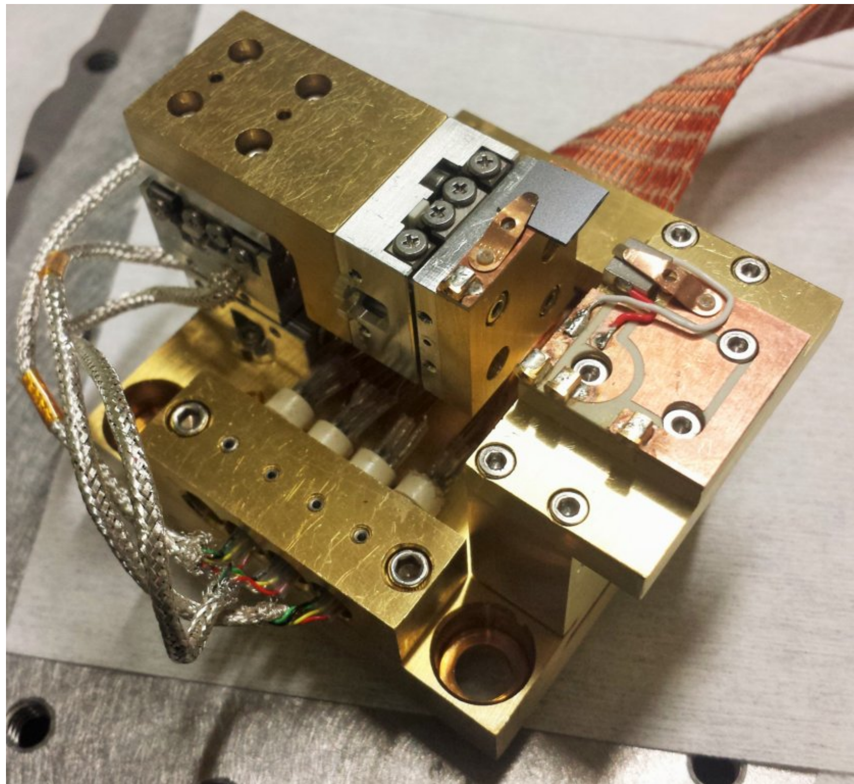

FIGURE 3.6. Platform for nanopositioner stages. This platform is used to mount the three stages for the X, Y, and Z movement axes. Each stage is controlled through the microconnectors, shown on the lower left edge of the platform. The Z stage is rotated 90 degrees using an L-shaped connector. The small grey square is a piece of gold covered silicon which is used as an anode. On the right is the probe holder mounted on an upright to bring it to the same height as the anode. The electrical connections to the platform were made using a ribbon cable, shown in the top right.

Three stages (for X, Y, and Z) were mounted on a platform, shown in Figure 3.6 for three dimensional movement of the sample. The probe was mounted in the probe holder, on top of an upright piece to put it at approximately the same height as the sample/anode when the stages were zeroed. On the bottom side is a series of micro connectors to drive the stages and to connect to the probe and piezo. On the top side is an element for strain relief of the ribbon cable. Underneath the platform (not shown) is a dovetail connector for mounting the platform in the SEM, FIB, or vacuum chamber described above.

3.5. SmarAct Stages

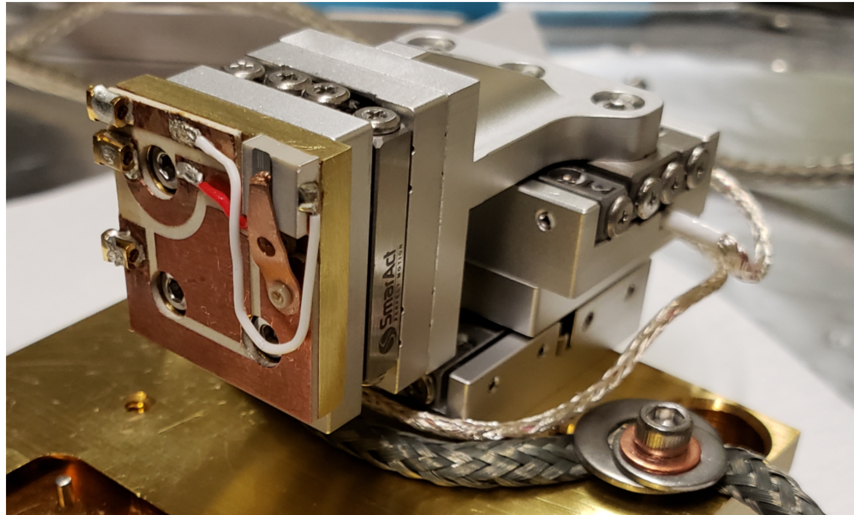

FIGURE 3.7. Stack of Smaract nanopositioning stages. This is a stack of two SLC1730 stages for X and Y positioning, and an SLC1720 stage for Z positioning. These stages are closed loop with a resolution of 1 nm. Due to the closed-loop nature, these stages were used for the later scanning experiments.

For later scanning measurements, we wanted absolute positioning in X and Y, so we acquired new closed-loop stages from Smaract. These stages had a similar footprint to the Micronix stages, but with an internal optical encoder for closed loop feedback. The set consisted of two SLC1730 stages for X and Y positioning, and an

SLC1720 stage for Z positioning. All of these stages have a resolution of 1 nm using the MCS-2 control unit. The 1730 have a travel range of 21 mm, while the 1720 has a travel range of 12 mm. The 1730 stages have an extra U-shaped body piece to increase their mechanical stability.

3.6. Probe Holder

The probe holder, shown in Figure 3.8, is a printed circuit board (PCB) epoxied to a piece of brass for mechanical stiffness. The PCB traces were milled out using a desktop CNC machine. The piezo (MMech NAC2013) for driving the cantilever is located in the corner so the probe is projected out into free space, allowing for better access to samples and for imaging in the SEM/optically. The electrical connection to the probe is made using a copper-beryllium spring/clip. There is a small screw underneath the clip that will lift the clip off of the probe when it is unscrewed. All of the wires in the vacuum chamber end in pins that plug into the sockets soldered to the PCB. The holes in the probe holder are spaced by 10 mm to attach to the mounting holes on the face of the Z nanopositioner stage.

The probe holder is mounted to the nanopositioner during the CNT attachment. The CNT sample is mounted upside down under the small clip. This orientation allows for a smaller working distance in the SEM during probe fabrication, discussed in Chapter IV. The probe holder is mounted face down at a slight angle in the vacuum chamber for scanning/measuring samples. This gives the probe more clearance such that only the CNT should contact the sample. These are both shown in Figure 3.9.

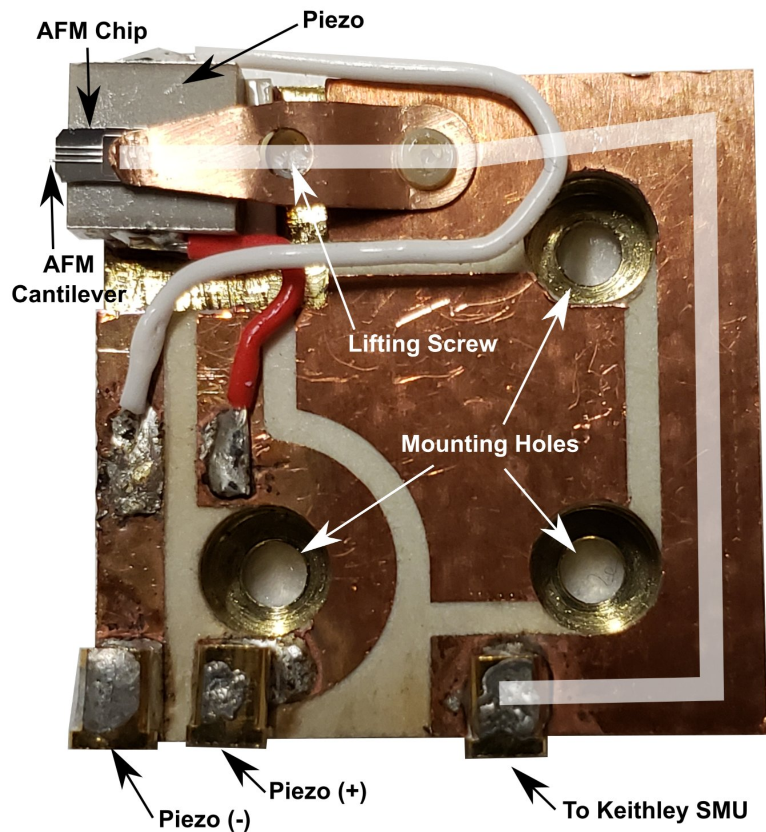

FIGURE 3.8. Probe holder. The PCB on the probe holder allows for easier electrical connections to the piezo and the probe. The electrical connections are made by horizontal pin sockets soldered to the PCB and the connecting wires terminate in pins. The position and orientation of the piezo allows for the AFM cantilever to project further out into free space for better clearance when performing measurements. The AFM chip is mounted on top of the piezo (MMech NAC2013) and is held in place by a copper-beryllium spring. This spring also makes electrical contact with the AFM chip. Underneath the spring is a lifting screw that lifts the spring when unscrewed. The mounting holes are spaced 10 mm apart for attaching to the nanopositioners.

3.7. Piezo Calibration

The specification for the piezo chip is an expansion of 22 nm for an applied bias of 1 V. To test that this was accurate, we imaged the edge of an AFM tip attached to the piezo in the SEM. While imaging, we applied a slow (1 Hz) voltage oscillation with an amplitude of 16 V peak to peak. This resulted in the edge of the AFM

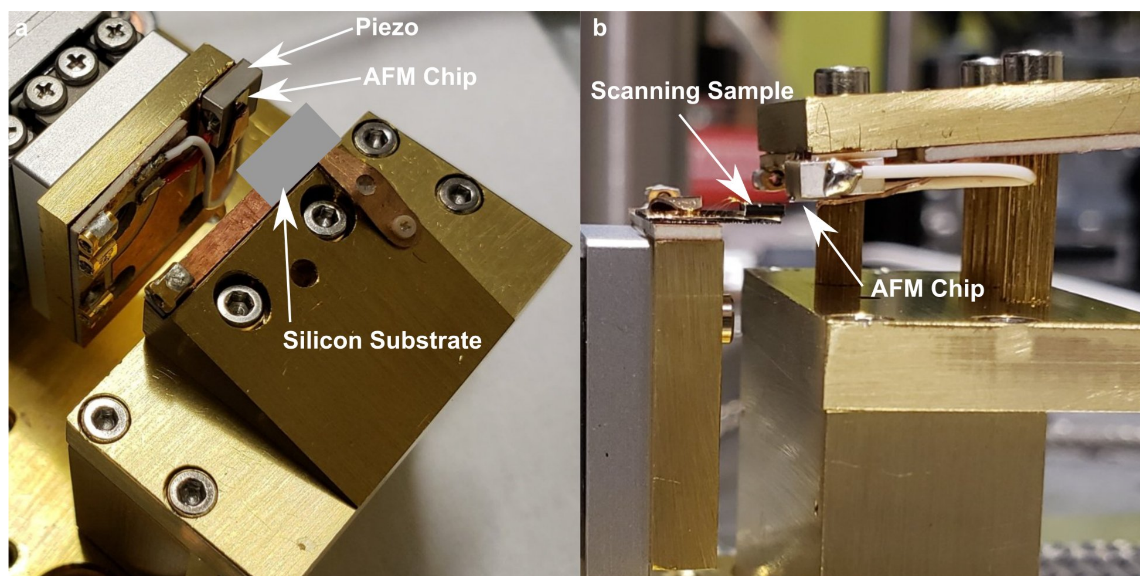

FIGURE 3.9. (a) Probe holder set up for attachment of CNT to AFM tip. With this orientation, the working distance in the SEM can be reduced for better imaging and a lower chance of impacting the pole piece. The grey box represents the location of the cleaved silicon substrate carrying the CNTs. (b) Probe holder set up for scanning samples. The slight downward angle allows for more clearance for the probe to access the sample.

tip moving by 328 nm peak to peak. The resulting calibration for this piezo is then 20.5 V/nm, very close to the specification.

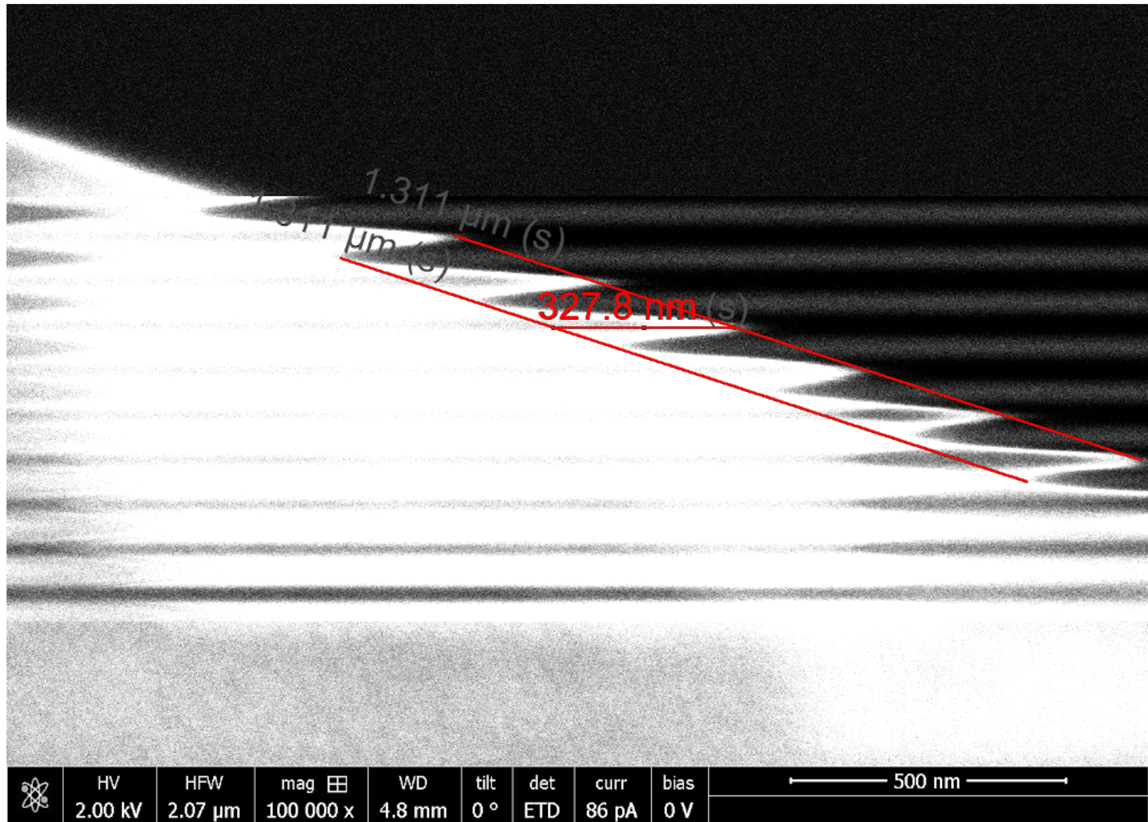

FIGURE 3.10. Calibration of slow displacements using the piezo. This figure shows an SEM image of the edge of an AFM tip that is oscillating from left to right. The image was taken using a very slow scan rate. By making a line along the two extremes of the oscillation, we can measure the amplitude of (328 ± 30) nm peak to peak. The piezo moving the AFM tip was driven with a 16 V peak to peak signal at 1 Hz, giving a calibration of (20.5 ± 1.9) V/nm. This is close to the specification for this piezo of 22 V/nm.

CHAPTER IV

PROBE FABRICATION

The key component of my displacement measurement platform is a single carbon nanotube. This requires a device which can make electrical contact to the nanotube and be positioned in a controlled manner. In this chapter, I describe my fabrication method, in which I position a single, carefully selected carbon nanotube onto a metal coated AFM tip and cement them together using in situ metal deposition. The use of a standard AFM probe as a base allows for a simple platform for moving the probe and making electrical contact to the nanotube field emitter.

4.1. CNT Sample

The carbon nanotubes we are using for the probes are multi-walled carbon nanotubes grown by the arc discharge method at UC Berkeley. The nanotubes have a length of 1-10 µm and a diameter of ∼10 nm. We place a thread from the arc discharge sample into a vial filled with isopropyl alcohol, and then sonicate the solution for 5 minutes to separate the nanotubes. The solution is then deposited on a gold-coated silicon substrate and allowed to dry. The substrate is coated with gold (before depositing the nanotubes) to prevent charging during imaging with an electron microscope.

Immediately before the assembly of the probe, the silicon substrate is cleaved into two pieces to create a sharp edge By doing this, there is a high probability that some carbon nanotubes will be cantilevered off the edge into free space. Only the piece of the substrate with a negative side wall (undercut) is usable when trying to image the CNTs. This technique produces approximately 10 well separated

(not clumped together) nanotubes on a single sample. The cleaved sample is then mounted to the nanopositioner platform.

4.2. Assembly of Probe

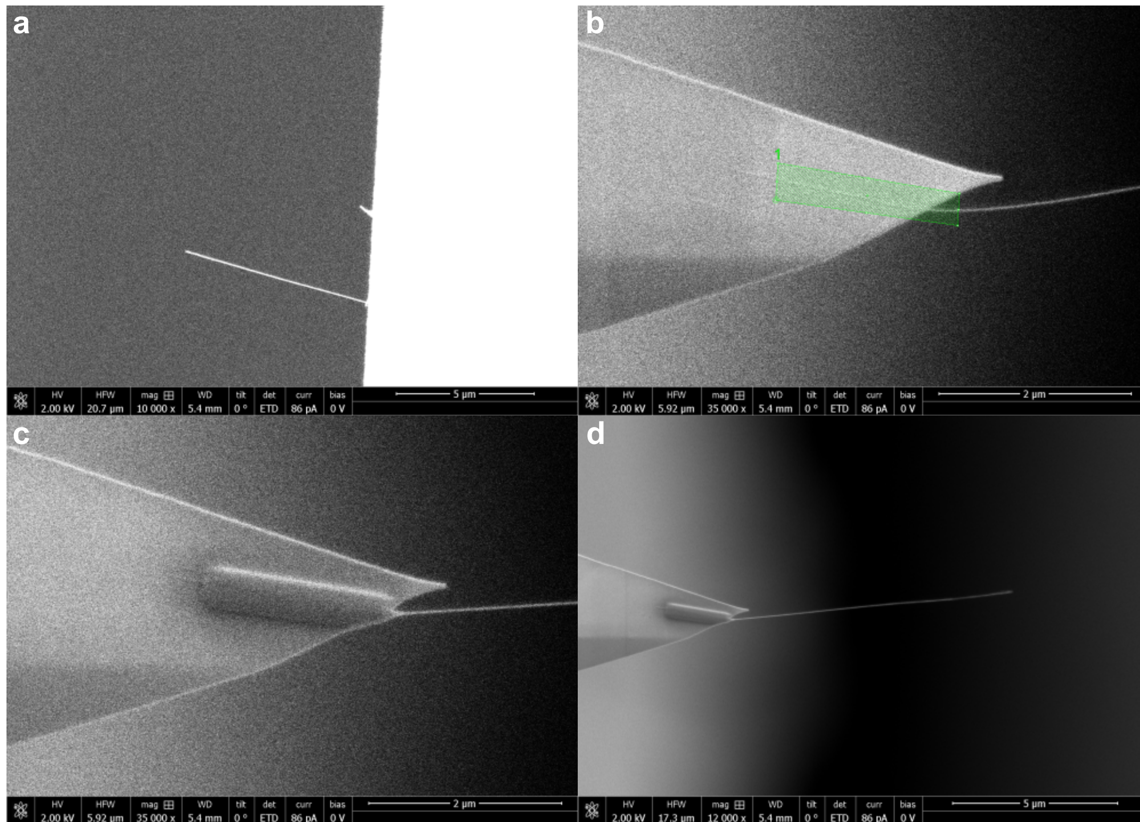

FIGURE 4.1. Assembly steps for a CNT probe. (a) A single carbon nanotube is projected off the edge of a cleaved piece of silicon. (b) The CNT is in contact with the AFM tip. The green shaded box represents where the electron beam will be scanned to deposit the platinum. (c) Platinum is deposited on the AFM tip, securing the CNT in place. (d) The final probe after the CNT has been pulled off of the silicon surface. For this probe, the final CNT length was 8.5 µm. Probe 52.

We begin the assembly process by inspecting the cleaved edge using a scanning electron microscope (SEM), typically using low beam energy (2 keV) and low beam currents (86 pA), to locate the separated nanotubes. These beam parameters make it easier to see low-Z materials, like carbon, and decrease the amount of contamination

deposited on the CNT. If there is too much contamination, the attachment procedure could fail. An example of this is shown in Figure 4.1a. Once a suitable nanotube is identified, we use the nanopositioner platform (discussed in Section 3.4) to position the tip from an AFM probe (μmasch HQ:NSC35/PT) near the nanotube and bring it into focus. From there, small adjustments are made until the tip contacts the nanotube (Figure 4.1b). Once contact is made, we use electron beam induced deposition of metal to glue the nanotube to the AFM tip. For this process, an organo-metallic gas carrying platinum is injected into the SEM and the molecules are adsorbed onto nearby surfaces. The electron beam is then scanned over the area of interest and the secondary electrons "crack" the molecules, leaving metal behind, as shown in Figure 4.1c. After this, the AFM tip is moved away from the edge of the substrate, pulling the nanotube with it (Figure 4.1d). A finished probe showing the entire AFM tip with attached carbon nanotube is shown in Figure 4.2.

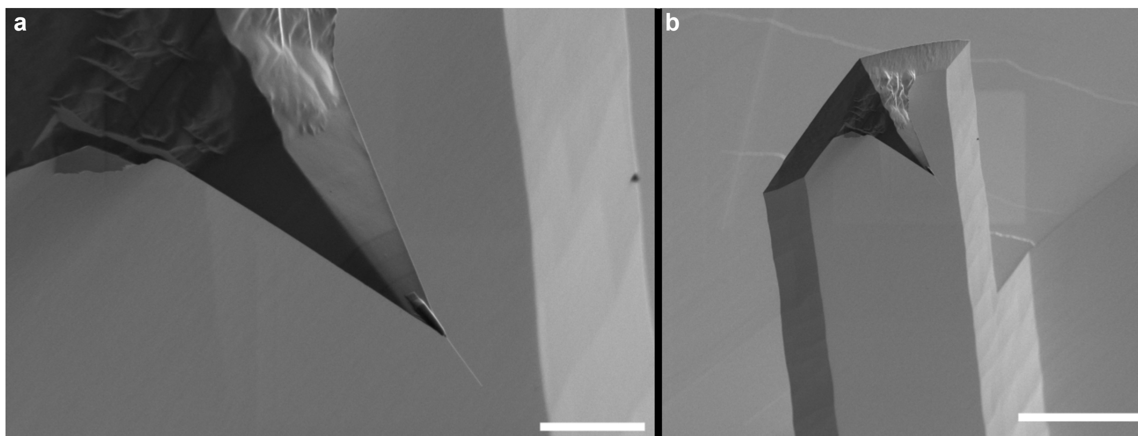

FIGURE 4.2. Finished field emission probe. (a) An SEM image of a CNT tipped field emission probe. This view shows the entire AFM tip with the CNT at the end, which looks like a pale line. The platinum used to attach the CNT is visible at the end of the AFM tip. The length of the CNT for this probe was 2.4 µm. Scale bar is 4 µm. (b) A zoomed out view showing the entire AFM cantilever. The scale bar for this part is 20 µm. Probe 45.

We were able to successfully attach a CNT to the AFM tip approximately 80% of the time. The average length of the nanotube extending from the tip was (4.6 ± 2.1) µm, with a maximum of 11 µm and a minimum of 1.6 µm. However, because these probes were fabricated in the SEM, we cannot tell if the CNT has a significant angle out of the plane of focus. In a few cases, we were able to apply a bias to the probe while inside the SEM and observed the CNT increase in apparent length by ∼500 nm. With a good CNT sample to pull from, we were able to fabricate good probes (measure consistent field emission) approximately 66% of the time.

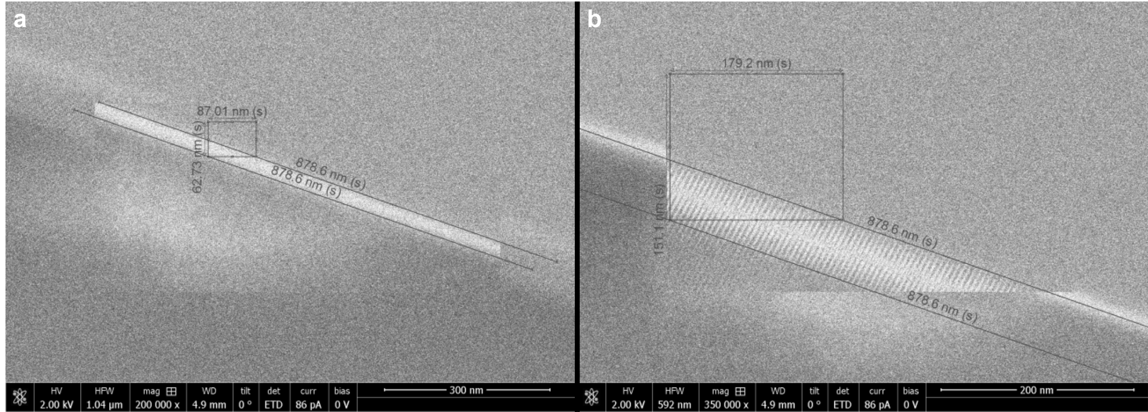

FIGURE 4.3. Calibration of probe oscillation amplitude. To measure the amplitude of the probe, we drove the cantilever on resonance ($f_0 = (198\,048 \pm 1)\,\mathrm{Hz}$) and imaged the edge of the AFM tip using the SEM. With the right imaging speed, the edge will appear to be a standing wave. (a) With no driving applied, the edge of the AFM tip appeared to be a thick white band, with a width of 87 nm in the horizontal direction. (b) With a driving amplitude of 1 mV, the white band had a peak to peak amplitude of 179.2 nm in the horizontal direction. This results in a physical vibration amplitude of $(179.2 - 87)/2 = 46.1\,\mathrm{nm}$. Probe 61.

4.3. Probe Transport

After fabrication, we would first ground ourselves using a grounding strap. Then, the piezo platform was removed from the FIB and placed in a box lined with copper tape to reduce the probability of electrostatic discharge destroying the nanotube.

This box was transported back to our lab, where we again grounded ourselves before removing the platform from the box. The platform was then loaded into the vacuum chamber for characterization.

4.4. Probe Characterization

The metal from the electron beam induced deposition process tends to be contaminated with organic materials and carbon which could produce a poor electrical contact between the AFM tip and the CNT. To clean this up, we can anneal the contact by running current through the tube and heating it up. When the tip of the carbon nanotube first makes contact with the anode (a gold coated silicon chip), the resistance is on the order of $100\,\mathrm{k\Omega}$. A small bias is applied using a Keithley 2450 source-measure unit (SMU) to start current flowing. As the contact anneals, the current will slowly increase while maintaining the same bias value. After running $\sim 100\,\mu\mathrm{A}$ for several minutes, the resistance usually drops to below $10\,\mathrm{k\Omega}$. An typical example of current-voltage curves before and after annealing is shown in Figure 4.4.

The next piece of characterization we do is testing the field emission properties of the probe. To do this, we position the probe away from the anode and sweep an electrical bias (V_{dc}) while measuring the current (I). By plotting $\ln(I/V_{dc}^2)$ vs $1/V_{dc}$, we can create what is referred to as a Fowler-Nordheim curve. The hallmark of field emission occurs when this curve exhibits a negative slope, as shown in Figure 4.5. A simple current-voltage plot also shows the characteristic exponential form of field emission. For this particular probe, the onset voltage was $V_{dc} = 47\,\mathrm{V}$, which is denoted by the break in the FN curve. This curve also allows us to extract some

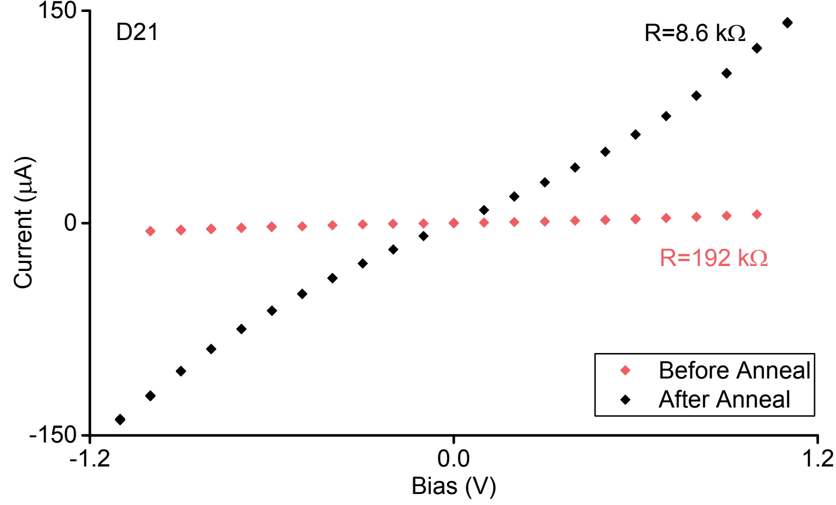

FIGURE 4.4. Current-Voltage curves before and after annealing. With the probe in contact with the anode, we can measure the IV characteristics of the probe. Immediately after fabrication, the resistance of the probe is $R = 192\,\mathrm{k}\Omega$ as shown by the red curve. As current flows through the probe, the parts with the highest resistance (like the metallic contact to the nanotube) will heat up. After some time, this contact is annealed and creates a better contact with the nanotube, lowering the resistance to $R = 8.6\,\mathrm{k}\Omega$ as shown by the black curve.

parameters about the emitter. By rearranging the Fowler-Nordheim equation into the form of $y = mx + b$, we get

$$\ln\left(\frac{I}{V_{dc}^2}\right) = -\frac{Bz}{\gamma}\frac{1}{V_{dc}} - \ln\left(\frac{z^2}{A\gamma^2}\right) \tag{4.1}$$

so we can solve for $\gamma = -Bz/m$, where m is the slope of the FN curve and $B = 7.3343 \cdot 10^{10}\,\mathrm{V/m}$. Note that, because the FN curve has a negative slope ($m < 0$), the field enhancement factor is still positive. The value of B comes from Equation 2.2 with $\phi \approx 5\,\mathrm{eV}$ as the work function for a carbon nanotube.

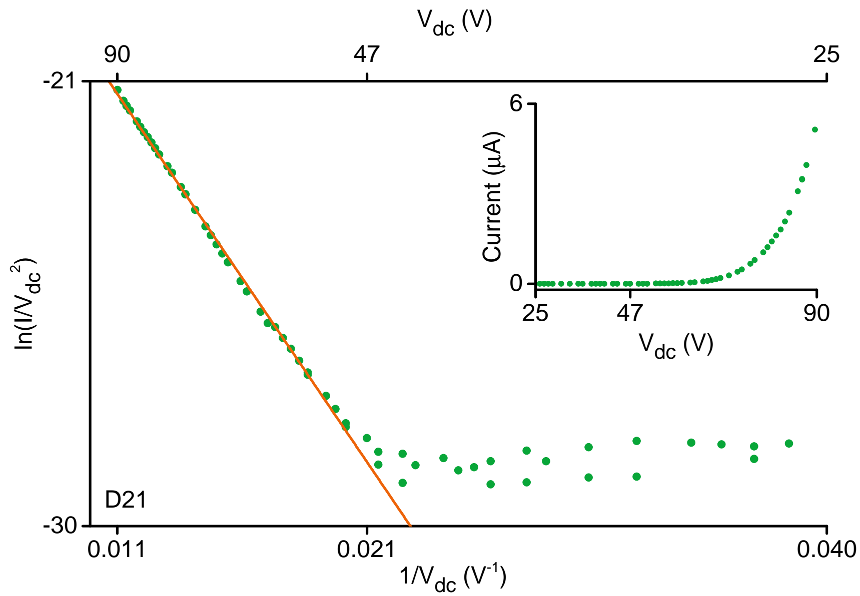

FIGURE 4.5. Fowler-Nordheim curve for a field emission probe. The negative linear slope is a key sign of field emission. The linear fit is of the form shown in Equation 4.1 giving a slope of $m = -733$, and an intercept of $b = -13$. Using these, we can calculate the field enhancement factor of $\gamma \approx 65$. The inset shows the standard current-voltage curve for field emission data. The threshold for field emission was at $V_{dc} = 47\,\mathrm{V}$, after which you can see the exponential increase in the field emission current. The very clear break in the Fowler-Nordheim curve occurs at the threshold of field emission. For this measurement the probe was at a gap of $z = 650\,\mathrm{nm}$

CHAPTER V

FIELD EMISSION DISPLACEMENT SENSING

The nanotube probes described in the previous chapters have a strong position-dependent field emission signal. This position dependence is expected to provide a means for high resolution displacement sensing. In this chapter, I measure the displacement sensitivity in three ways. First, I measure the sensitivity using the dc current from the carbon nanotube. Then, by leveraging the mechanical resonance of the AFM cantilever, I use resonance sensing as an alternative signal to the dc current via amplitude modulation. Finally, I track the resonator frequency using a phase locked loop via frequency modulation, greatly reducing the noise. Using this, I demonstrate sub-atomic displacement sensitivity of $\sim$280 fm/$\sqrt{\text{Hz}}$ with the probe $\sim$250 nm from the surface. As an application of this platform, I scan the probe to measure the surface topography of a nanostructured surface.

5.1. DC measurements

To start investigating the performance of the carbon nanotube enhanced Topografiner, we looked at the dc field emission as a function of the gap between the emitter and the anode. We found the position of zero gap by making contact between the CNT and anode while applying a bias, causing a current to flow, then moving the CNT away until the current dropped to zero. We positioned the emitter at $\sim$650 nm from the anode and started field emitting. We then increased the gap to $\sim$4.5 μm while measuring the dc current and pausing to take a resonance curve approximately every 50 nm. The results of this experiment are shown in Figure 5.1.

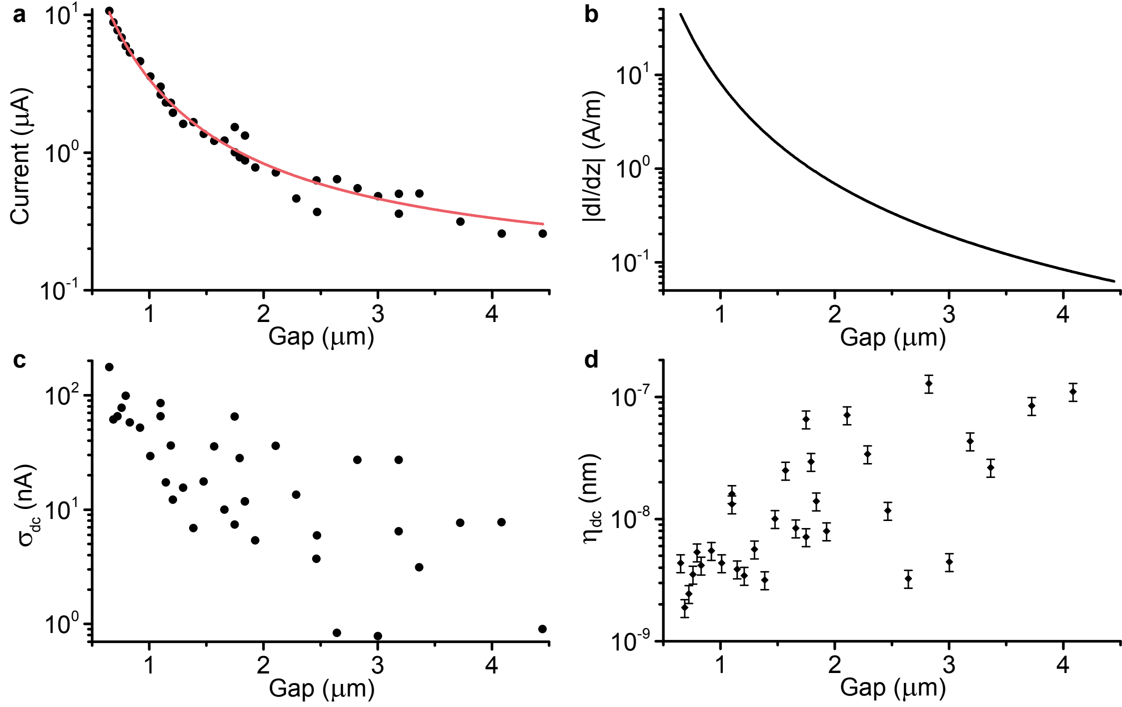

FIGURE 5.1. Displacement sensitivity using dc current. (a) The dc current as a function of the gap, starting at ~10 µA and finishing at ~0.25 µA. The data was fit using the Fowler-Nordheim equation (Equation 5.1) with a linearly varying field enhancement factor γ. (b) The derivative of the Fowler-Nordheim fit. (c) The noise from the dc current measurements. (d) The minimum measurable displacement using the dc current, calculated using Equation 5.2. Our best sensitivity was η_{dc}=(1.9 ± 0.3) nm. During these measurements, the dc bias voltage was V_{dc}=59 V.

In Figure 5.1a, we can see the exponential dependence of the current on the gap as in Equation 2.1, reproduced here in a simpler form for convenience:

$$I = A\frac{\gamma^2 V^2}{z^2}\exp\left(-B\frac{z}{\gamma V}\right) \tag{5.1}$$

where the field has been explicitly defined as F=$\gamma V/z$ and A and B are constants. At z=4 µm, the current is approximately 250 nA, and increases exponentially to 10 µA as the gap decreases below 1 µm. With this measurement, we now have a calibrated ruler, so given a current measurement, we know the position of the probe. The fit

in Figure 5.1a is done using the numerical form of the Fowler-Nordheim equation, Equation 2.2, with a modification to γ discussed below.

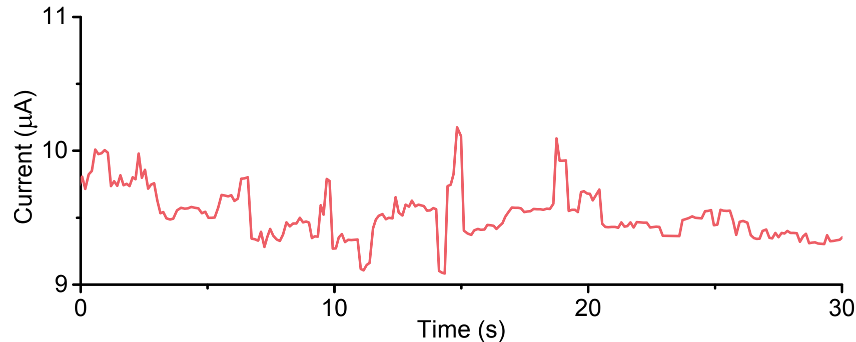

FIGURE 5.2. The dc field emission current tends to be very noisy. Due to its high sensitivity, it is easy to pick up mechanical vibrations from the environment. Along with this, there are often large, random jumps in the magnitude of the current. These are generally caused by ions or atoms landing on the emitter.

Unfortunately, the dc current is very noisy, as shown in the time series in Figure 5.2. The current has a tendency to have large jumps that can cause variations in the current of 10% or more. The noise is generally described as "flicker noise" and is likely due to ions and adsorbates landing on the carbon nanotube [36, 37]. Additionally, there could be long term drift, or even noise from mechanical vibrations in the environment.

If we measure this noise in the current, σ_{dc}, at each position, we can look at how it behaves as the gap changes, shown in Figure 5.1c. This noise clearly falls off exponentially with increasing gap, from 100 nA below 1 μm, and ending at 1 nA at 4 μm. On average, the noise is approximately 2% of the measured dc current.

We want to know how sensitive of a measurement we can achieve using the dc current. To do that, we can compare the noise in the current measurement to the rate of change in the current and find the dc sensitivity, η_{dc}.

$$\eta_{dc} = \frac{\sigma_{dc}}{|\partial I/\partial z|} \tag{5.2}$$

To find the rate of change in the field emission current, $|\partial I/\partial z|$, we can calculate the derivative of the fit obtained using the Fowler-Nordheim equation. This is shown in Figure 5.1b.

Combining all of this, we find how η_{dc} varies with the position, shown in Figure 5.1d. Even though the noise increases for small gaps, due to the exponential increase in the field emission slope, the trend in the sensitivity is to improve at small distances. Starting at a gap of 4 µm, the dc sensitivity is approximately 100 nm. Our best sensitivity was η_{dc}=(1.9 ± 0.3) nm at a distance of ∼650 nm. Even at 1000 nm though, we should still be able to measure displacements as small as 4-5 nm. Our best sensitivity is on par with the results from the Topografiner, however, we achieved this at a distance of 650 nm compared to only 10 nm, an increase of almost two orders of magnitude. From this result, it appears displacement sensing using dc field emission is limited by noise in the dc current.

5.1.1. Modifications to the Fowler-Nordheim Fit

Initially, when fitting the field emission data in Figure 5.1a using the Fowler Nordheim equation, we found the theory predicted the current should fall off much faster than the data shows. In reviewing the literature, we discovered some discussion that the field enhancement factor actually varies with position[33, 34] as discussed in Section 2.3. Between 100 nm and 10 µm in Figure 2.3, you can see that the change in γ is approximately linear. Adding this variation in γ allowed the fit to work almost perfectly:

$$\gamma(z) = \gamma(z_0) + \frac{\partial \gamma}{\partial z}(z - z_0) \tag{5.3}$$

Using the FN plots before and after this run, we found γ=172 at 650 nm, and γ=471 at 4.5 µm. The fit of the dc data required γ=186 at 650 nm, and γ=802 at 4.5 µm, which is within a factor of two compared to the measured value.

5.2. Lock-In Amplification

The simplest way to improve our displacement sensitivity would be to apply a filter to the dc current. One of the most powerful filters at our disposal is the technique of lock-in amplification. For this to work though, we need an oscillating signal that the amplifier can then lock into. In other words, we need to create an oscillating current at a fixed frequency. Due to the distance dependence of the current, one way to accomplish this is by oscillating the position of the probe. Fortunately, our emitter is attached to an AFM cantilever, which can be used as a mechanical oscillator.

The signal measured by the lock-in amplifier, R, is proportional to the amplitude of the oscillating current δI_z, due to a mechanical oscillation of size δz. The expression for this is the derivative of the Fowler-Nordheim equation, given by:

$$R(\omega) \propto \delta I_z = \frac{AV_0\gamma}{z_0^3}(2V_0\gamma + Bz_0)\exp\left(-B\frac{z_0}{\gamma V_0}\right)\delta z(\omega) \tag{5.4}$$

The mechanical oscillations are due to vibrations in the AFM cantilever, so the amplitude can be determined using the damped harmonic oscillator

$$\delta z(\omega) = \frac{f_0/\omega_0^2}{\sqrt{\left(1 - \left(\frac{\omega}{\omega_0}\right)^2\right)^2 + \left(\frac{\omega}{\omega_0 Q}\right)^2}} \tag{5.5}$$

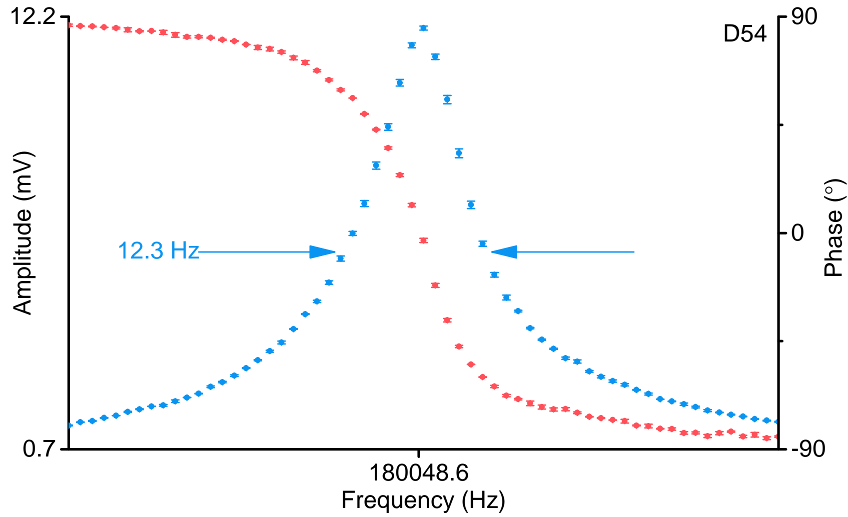

FIGURE 5.3. Example of resonance curve measured using field emission. The resonance frequency for this probe was f_0=(188 048.60 ± 0.06) Hz with a quality factor of Q=(2.54 ± 0.05) · 10^4. The peak amplitude for this curve was R=(11.89 ± 0.05) mV. During this measurement, the probe was at a gap of z=650 nm, the bias voltage was V_{dc}=59 V, and the average dc current was I_{dc}=(8.42 ± 0.12) µA. On resonance, this probe had an amplitude of ∼17.5 nm.

As an immediate test of the lock-in signal, we can measure the resonance curve of the AFM cantilever. We drive the mechanical vibrations by applying an ac voltage (sourced from the lock-in amplifier) to a piezo plate actuator on which the AFM chip is mounted. We then detect δI with a current preamplifier, which sends the signal into the lock-in amplifier as we sweep the frequency through resonance. A representative amplitude and phase curve near resonance are shown in Figure 5.3 where the physical amplitude of the cantilever was ∼17.5 nm on

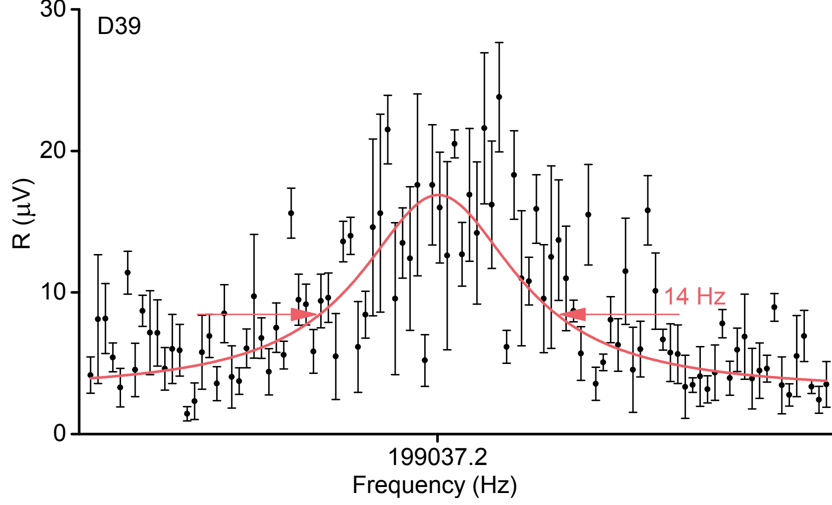

FIGURE 5.4. Measuring the thermal motion of the probe using field emission. Using Equation 5.6, the theoretical amplitude should be ~5 pm. The data was fit using a lorentzian to yield a resonance frequency of f_0=(199 037.2 ± 0.5) Hz with Q=(2.46 ± 0.44) · 10^4 and a peak amplitude of (16.9 ± 1.6) µV. The probe was at a gap of z=650 nm, the bias voltage was V_{dc}=83 V, and the average dc current during this measurement was I_{dc}=(11.2 ± 0.8) µA.

resonance. For this probe, we can extract a quality factor of $Q\sim26000$ and a resonance frequency of f=180 049 Hz, values that are consistent with the chosen AFM cantilever (Micromasch HQ:NSC35/PT) operated in vacuum. The resonance frequency was further verified by visual inspection with SEM (see Figure 4.3).

This technique is sensitive enough to transduce the thermal motion of the cantilever, as shown in Figure 5.4. The theoretical amplitude of the thermal peak should be:

$$S_z^{1/2} = \sqrt{\frac{4k_bTQ}{2\pi f_0 k}} = \sqrt{\frac{4(1.38\cdot10^{-23}\,\mathrm{J/K})(300\,\mathrm{K})(19810)}{2\pi(199\,038\,\mathrm{Hz})(9\,\mathrm{N/m})}} = 5.3\,\mathrm{pm}/\sqrt{\mathrm{Hz}} \qquad (5.6)$$

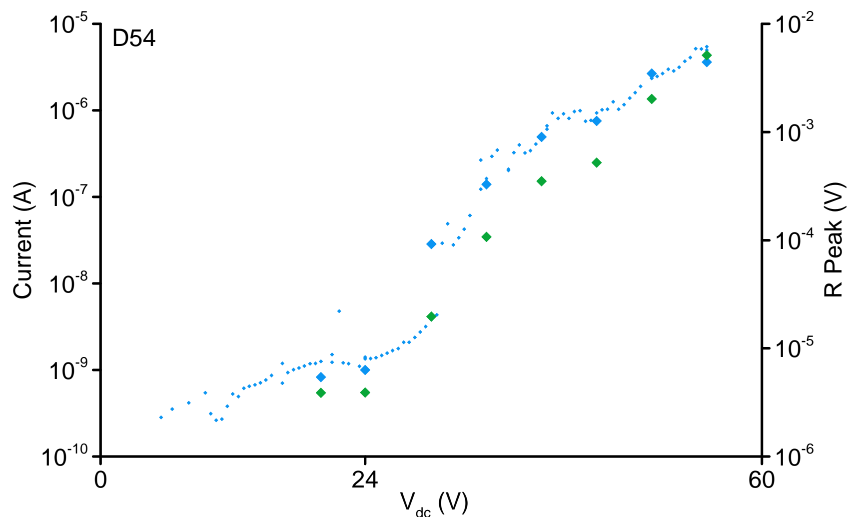

FIGURE 5.5. Confirmation that the resonance curves are measured by oscillations in the field emission current. The dc current is shown in the blue points using the scale on the right. The small points are from a voltage sweep to represent the general behavior of the field emission current. These measurements have a noise floor of approximately 1 nA, which can be seen for bias values below the field emission threshold of 24 V. After this, the current increases exponentially as the bias increases up to ∼5 µA at V_{dc}=55 V. Before the onset of field emission, there is no measurable resonance peak above the noise floor of ∼4 µV, represented by the green points. From there, the resonance curve amplitude rises by a factor of 1000 to reach peak R=5 mV. The large blue points represent the dc current measured concurrently with the resonance curve. These measurements were taken with a gap of z=650 nm. On resonance, the cantilever amplitude was ∼7 nm.

5.3. Verification of Field Emission Transduction

To confirm that the motion is transduced by field emission current, we concurrently measured the lock-in amplitude, R, and dc field emission current, I, for increasing voltage bias V_{dc} as shown in Figure 5.5. Below field emission onset at V_{dc}=24 V, both the amplitude, R, and current are at the noise floor for the lock-in amplifier and Keithley, respectively. At onset, both quantities rise quickly above the noise by a factor of 10 with only a small increase in the dc bias to 30 V. Both R and the current continue to rise steeply by an additional factor of ∼1000 at moderate bias levels (∼30 V above onset). The tight correlation between the amplitude and the current indicates that the motion is transduced by the field emission current, and rules out other potential transduction mechanisms, such as capacitive displacement current (CDC). We have measured resonance curves using CDC on probes that have lost their nanotube, but the required bias was increased to V_{dc}=200 V and the oscillation amplitude of the AFM cantilever increased to 100s of nm.

5.4. Lock-In Enhanced Topografiner

In order to investigate the position dependence of the ac measurement, we can measure a resonance curve at each position as we change the gap. Extracting the peak values from these resonance curves yields an alternative signal to measure small displacements. Like the dc field emission current, this signal exhibits an exponential dependence on the gap, according to Equation 5.4. This dependence is shown by the white points in Figure 5.6.

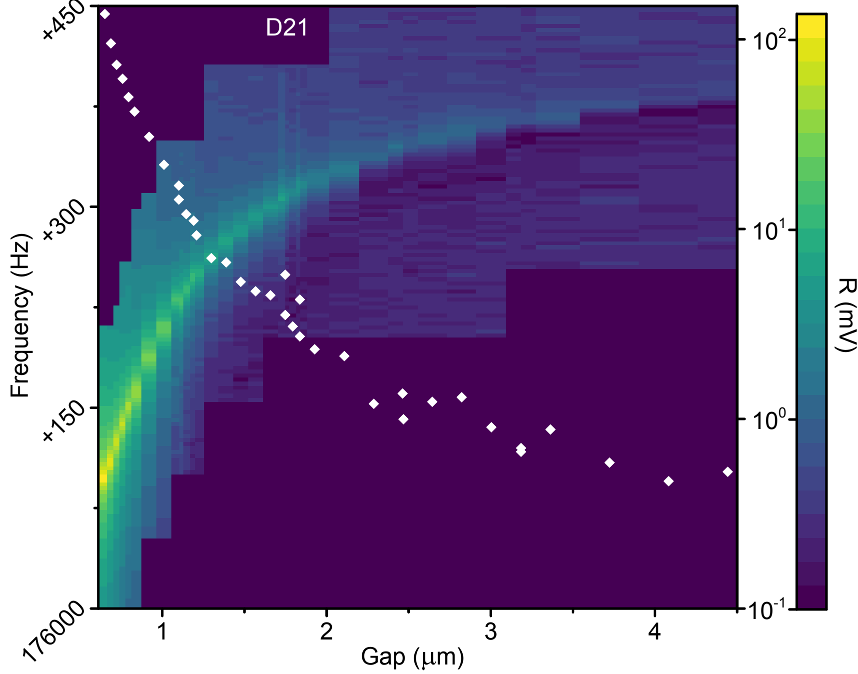

FIGURE 5.6. Spectrogram of resonance curves and peak R values in white. A resonance curve was measured approximately every 50 nm. Each vertical stripe in the spectrogram represents one resonance curve, with the amplitude shown by the color scale to the right. The white points represent the peak R value from each resonance curve using the scale on the right. The peak R increases exponentially from just below 1 mV to 100 mV as the gap decreases. From these measurements, it is easy to see the resonance curves shifting in frequency as the gap decreases, and the shift increasing in magnitude. The frequency shifts are discussed more in depth in the next chapter. During these measurements, the dc bias was V_{dc}=59 V. The dc current is shown in Figure 5.1 and ranged from ~0.25 µA to ~10 µA.

From this, we can calculate the sensitivity to displacements in the same manner as the dc current

$$\eta_R = \frac{\sigma_R}{\mid \partial R/\partial z \mid}\sqrt{\tau} \tag{5.7}$$

where σ_R is the noise in the amplitude measurement at the peak of the resonance curve, and τ is the measurement time, which determines the bandwidth of the lock-in amplifier. The noise in the amplitude measurement is found by taking multiple samples of the lock-in output while driving at a given frequency and measuring their

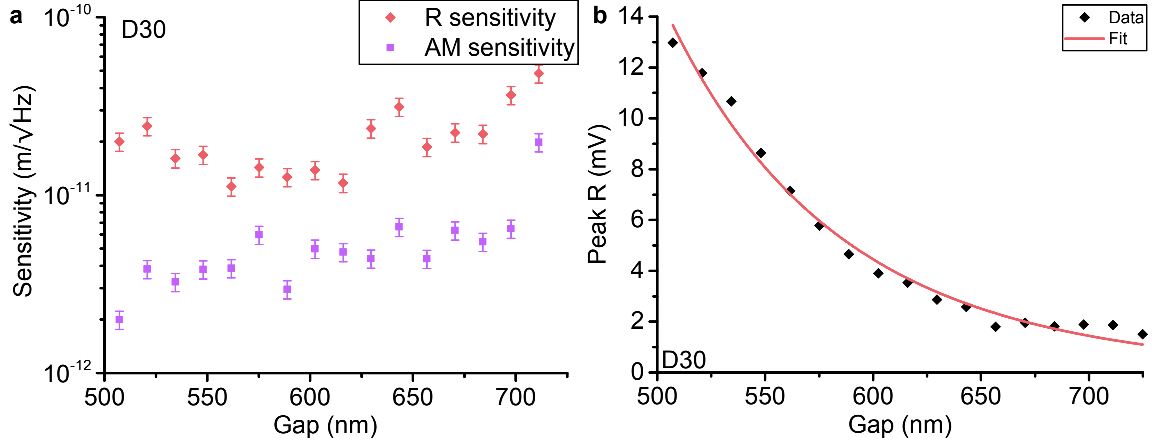

FIGURE 5.7. Displacement sensitivity measured using peak R and AM techniques. (a) The displacement sensitivity measured using the peak R, η_R (upper red diamonds). This uses the fit of Equation 5.4 to calculate $\partial R/\partial z$. The lower set of points (purple squares) shows the sensitivity when taking into account the frequency shift, η_{AM}. The R sensitivity starts getting worse for z<550 nm, most likely due to amplitude noise in the dc current caused by field evaporation. Using the AM technique improves the displacement sensitivity by a factor of five on average, but can shows order of magnitude improvements when η_R becomes more affected by amplitude noise. The best sensitivity value we measured using either of these techniques was η_{AM}=(2.0 ± 0.2) pm/$\sqrt{\text{Hz}}$ at z=507 nm. (b) The peak R extracted from the resonance curves and a fit using Equation 5.4. For these measurements, the dc bias was V_{dc}=100 V and the dc current ranged from 7 µA to 20 µA.

distribution. We can extract $\partial R/\partial z$ by fitting the peak R values using Equation 5.4, as shown in Figure 5.7b.

At a gap of approximately 700 nm, the sensitivity is η_R=(48.2 ± 5.7) pm/$\sqrt{\text{Hz}}$. From there, it decreases to η_R=(11.2 ± 1.3) pm/$\sqrt{\text{Hz}}$ at 560 nm, as shown by the red points in Figure 5.7a. Due to the reduced noise in this ac measurement technique, our sensitivity to displacements is improved by two orders of magnitude over the dc sensitivity. Unfortunately, this signal is proportional to the field emission current as seen by rewriting Equation 5.4,

$$R \propto \left(\frac{2}{z_0} + \frac{B}{V_0\gamma}\right) I(z_0, V_0)\delta z \tag{5.8}$$

This means that even though the lock-in amplifier is able to filter much of the noise at frequencies away from the resonance frequency, it is still affected by noise caused by changes in the amplitude of the current.

5.5. Amplitude Modulation

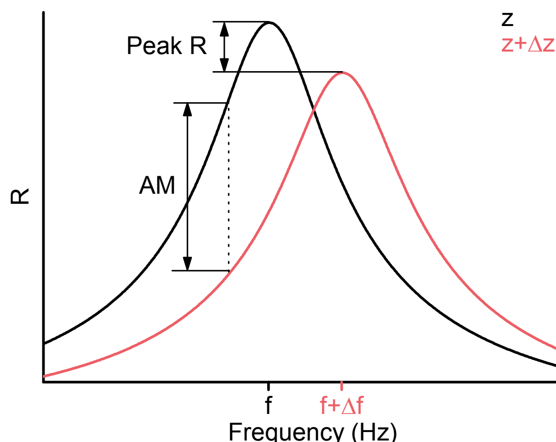

FIGURE 5.8. Two curves demonstrating Peak R and AM measurements. For two resonance curves taken at z (black) and $z + \Delta z$ (red), the signal for the peak R measurement would only take into account the change in height of the two peaks. Due to the additional frequency shift, if we measured R at a constant frequency, we get a much larger signal, denoted by AM, and therefore larger signal-to-noise. There is a trade off though with a decrease in dynamic range. If the red curve were to shift too far, the AM signal would become more or less constant and therefore unusable as a measurement of displacement.

Further increases in the sensitivity are achieved by using this system as a resonance sensor. A resonance sensor is a sensing instrument which relies on the mechanical resonance shifting in frequency in response to external stimuli. The most common example of this would be a resonant mass sensor, where any extra mass deposited on a mechanical resonator will shift its frequency.

In our case, as the AFM cantilever vibrates, a capacitive electromechanical coupling between the anode and cantilever is produced. This coupling modifies the

effective spring constant of the AFM cantilever, causing a shift in the resonance frequency. The frequency shifts can be observed in Figure 5.6. This figure shows a spectrogram of resonance curves (each vertical line) as a function of the gap. The amplitude of the resonance curves is indicated by the color, which is on a log scale. The resonance frequency of these curves is shifted towards a lower frequency as the gap is decreased. Further discussion of the origin of these frequency shifts can be found in Chapter VI.

By combining the position dependent frequency shift with the sharp slope of the resonance curve, we have a system that is incredibly sensitive to small displacements. An example of this is shown in Figure 5.8. For this to work, the resonator would be driven at a constant frequency away from the resonance and the amplitude measured. This frequency would correspond with the point where the slope of the resonance curve is steepest. As the resonance curve shifts in frequency, there is a much larger shift in amplitude compared to the shift in the peak R value. In this example, it would be approximately a factor of 3 increase in the signal. Unfortunately, this does come with a decrease in dynamic range because the signal will become relatively insensitive to displacements if the resonance curve shifts too far. When including resonance effects, the sensitivity becomes

$$\eta_{AM} = \frac{\sigma_{AM}\sqrt{\tau}}{\max\left|\frac{\partial R}{\partial z}\right|} = \frac{\sigma_{AM}\sqrt{\tau}}{\max\left|\frac{\partial R}{\partial \omega_0}\frac{\partial \omega_0}{\partial z}\right|} \tag{5.9}$$

where σ_{AM} represents the noise in the measurement of R at the maximum slope of the resonance curve (as opposed to the peak), τ is the time constant of the lock-in, and

$$\max\left|\frac{\partial R}{\partial \omega_0}\frac{\partial \omega_0}{\partial z}\right| \propto \frac{(1+\sqrt{2}Q)}{\omega_0}R(\omega_m)\frac{\partial \omega_0}{\partial z} \tag{5.10}$$

represents the combination of the maximum slope on the resonance curve ($\partial R/\partial\omega_0$) and the slope of the resonance frequency as a function of the gap ($\partial\omega_0/\partial z$). Here, $R(\omega_m)$ is given by Equation 5.4.

The AM sensitivity as a function of gap is shown in the lower set of points (purple squares) of Figure 5.7a. If we extrapolate out to 1 µm, the sensitivity would be $\eta_{AM}{\approx}50\,\mathrm{pm}/\sqrt{\mathrm{Hz}}$. Our best displacement sensitivity using this technique was $\eta_{AM}{=}(2.0 \pm 0.2)\,\mathrm{pm}/\sqrt{\mathrm{Hz}}$ after the gap has decreased to 500 nm. Incorporating the frequency shift improves the sensitivity by a factor of 5 or more compared to only measuring shifts in the peak amplitude and is three orders of magnitude better than the dc results.

5.6. Frequency Modulation

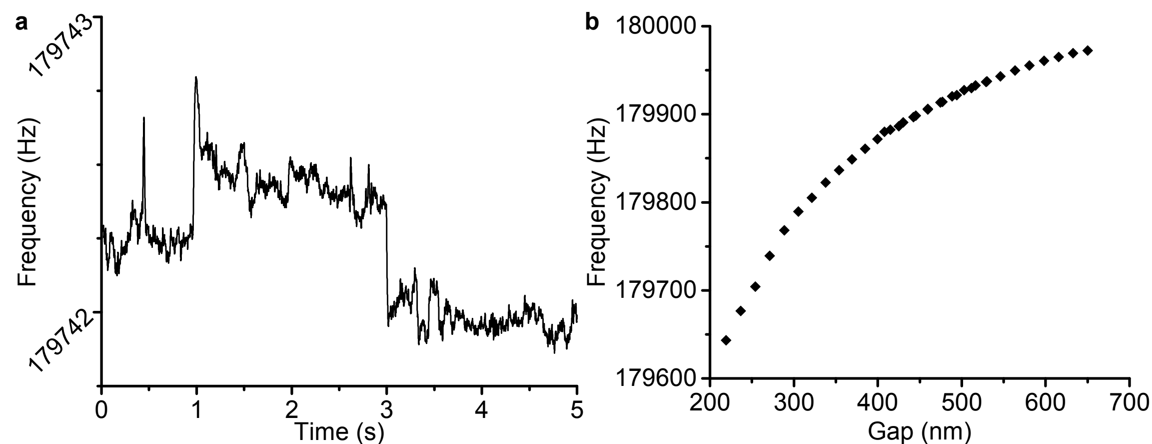

FIGURE 5.9. The frequency as measured by the PLL has some amount of noise, but it varies on average less than a part per million, on the order of 100s of mHz. The frequency ranges from 179 975 Hz to 179 650 Hz as the gap decreases. The shifts in frequency increase in magnitude as the gap decreases. Ideally this would lead to higher sensitivities at smaller gaps.

In order to avoid all of the amplitude noise, we can pivot to a completely different method of measuring the position of the probe. In this method, we measure the

frequency of the resonator directly using a phase locked loop (PLL). A PLL is an incredibly powerful technique that allows you to drive the resonator at a fixed phase, rather than a fixed frequency. This means that even if the resonance frequency changes, you can always be driving at the same position on your resonance curve. In our case, we choose a phase that allows us to drive on resonance. This gives us the cleanest signal for the lock-in and PLL to measure. Figure 5.9a shows the output of the PLL measurement as a function of time. The average noise in this measurement is extremely low, less than a part per million. This results in frequency noise of 10s to 100s of mHz. Using the PLL, we can measure the frequency as a function of the gap, $f(z)$, as shown in Figure 5.9b. We see that the frequency shifts become larger as the gap decreases in an accelerating manner. Like the exponential growth of the dc current, this will hopefully lead to better sensitivities as the probe approaches the anode.

We determine the FM displacement sensitivity (η_{FM}) using the expression

$$\eta_{FM}(z) = \frac{\sigma_f \sqrt{\tau}}{\mid \partial f / \partial z \mid} \tag{5.11}$$

where σ_f is the frequency noise, and τ is the integration time of the measurement. We measure $\partial f / \partial z$ directly by looking at the frequency shift for a step in the position of the probe. From Figure 5.9b, we see that the magnitude of $\partial f / \partial z$ increases close to the surface, so that the sensitivity should improve with decreasing z.

We obtain the noise at a given frequency $f(z)$ by first measuring the Allan deviation [38].

$$\sigma_a(\tau) = \sqrt{\frac{1}{2(N-1)} \sum_{1}^{N-1} \left(\frac{\bar{f}_{i+1} - \bar{f}_i}{f_0} \right)^2} \tag{5.12}$$

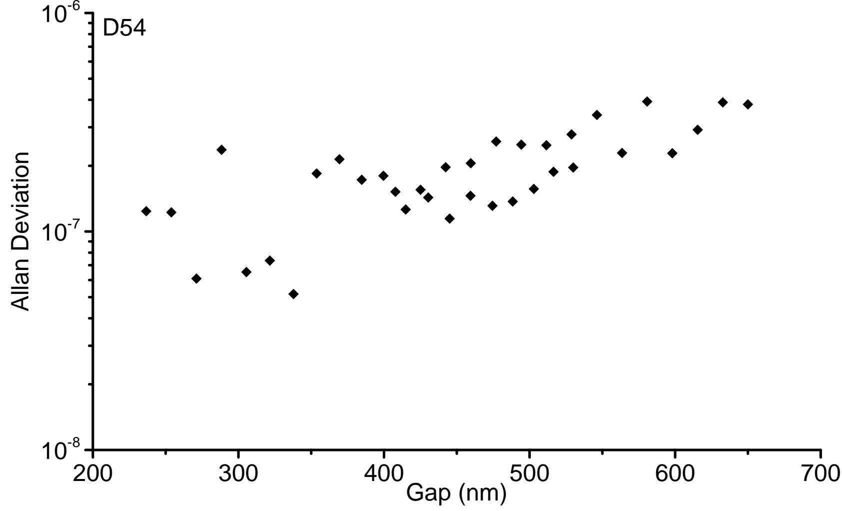

FIGURE 5.10. Allan deviation for FM displacement sensitivity measurement. For each gap position, the Allan deviation was measured using 5 s of data with a time constant of τ=2.7 ms. The deviations measured here range from 10^{-6} to 10^{-7} as the gap decreases. In order to find the frequency noise, the Allan deviation has to be combined with the average frequency during the measurement.

The Allan deviation is a method of measuring frequency fluctuations by averaging time data using a set integration time, τ, and looking at the difference between adjacent averaged samples. The frequency noise is then calculated using $\sigma_f = \sigma_A(z)f(z)$. Measured values of the Allan deviation were generally between 10^{-7} and 10^{-6} for this data set, shown in Figure 5.10.

By combining the frequency noise and frequency shifts, we calculate η_{FM}, shown in Figure 5.11. The sensitivity $\eta_{FM}(z)$ decreases rapidly below $z \sim 1$ µm, starting with $\eta_{FM} \sim 20\,\mathrm{pm}/\sqrt{\mathrm{Hz}}$ at $z \sim 700$ nm On a point by point basis, our best sensitivity was $\eta_{FM} \sim 280\,\mathrm{fm}/\sqrt{\mathrm{Hz}}$ at $z \sim 270$ nm. This is based off of actual noise in the frequency measurement for that position. However, there are clearly other sources of noise that have caused a large spread between adjacent measurements of the sensitivity. To account for the spread, we can take the mean of the final five points to find a value

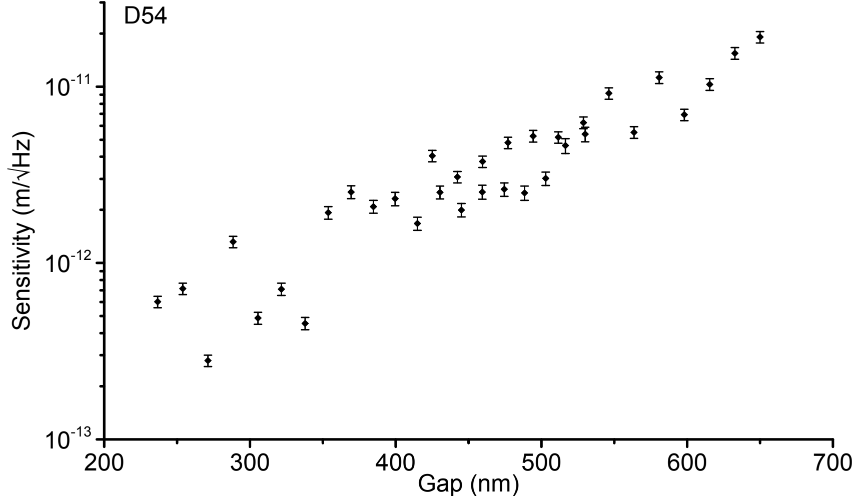

FIGURE 5.11. Noise equivalent displacement measurement using FM technique. While driving the probe on resonance using a PLL (BW=27 Hz), the probe was moved closer to the anode with steps of approximately (16.5 ± 1.2) nm. For each step, the frequency shift was measured and compared with the frequency noise given by the Allan deviation. At z=650 nm, the displacement sensitivity was $\eta_{FM}=(19.1 \pm 1.4)\,\mathrm{pm}/\sqrt{\mathrm{Hz}}$. On a point by point basis, the best sensitivity of $\eta_{FM}=(280 \pm 21)\,\mathrm{fm}/\sqrt{\mathrm{Hz}}$ was measured at a gap of z=270 nm. The main source of noise in the reported sensitivities was the uncertainty in the step size. For these measurements, the dc bias was V_{dc}=60 V and the dc current ranged from 4 µA to 20 µA. The amplitude of the probe oscillations was 17.5 nm. At z=220 nm, the field enhancement factor was γ=34.

that more accurately represents the displacement sensitivity with this technique. The result of this is $\eta_{FM}=(7 \pm 4) \cdot 10^2\,\mathrm{fm}/\sqrt{\mathrm{Hz}}$.

Below a gap of 270 nm, the downward trend of η_{FM} flips and the sensitivity begins to worsen because of an increase in frequency noise. At these close distances, the large electric fields could begin to evaporate the CNT [39], thereby destabilizing the emission current and the frequency, leading to higher noise and worse sensitivity. Immediately after this run, the electric field was F=9.3 V/nm, which is just below the limit where field evaporation should start [39]. We can conclude then that field evaporation was occurring at these low gaps, serving to lower the local electric field until it was under the limit. Our best value of η_{FM} outperforms the original

Topografiner by over four orders of magnitude, while operating 10-100 times farther from the surface.

5.7. Slow Displacement Measurements

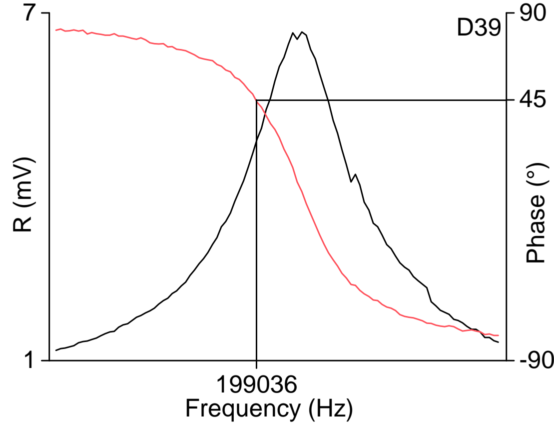

FIGURE 5.12. Before the slow displacement measurement, we measured the resonance curve to determine the driving frequency for a resonance style measurement. The black curve shows the the amplitude measured by the lock-in amplifier, with a peak of $R{\sim}7\,\mathrm{mV}$. The red curve shows the phase relative to the driving signal. The resonance frequency was $f_0{=}199\,041\,\mathrm{Hz}$. The steepest part of the curve is approximately 45° off resonance, at $f{=}199\,036\,\mathrm{Hz}$. For this measurement, the probe was at a gap of $z{\sim}680\,\mathrm{nm}$, the bias voltage was $V_{dc}{=}83\,\mathrm{V}$, and the average dc current was $I_{dc}{=}12\,\mu\mathrm{A}$.

We can use our nanotube topografiner as a dynamic micrometer to measure the motion of the base of the cantilever using both of these measurement techniques. For the AM method, we drive the cantilever at a constant frequency located at the steepest part of the resonance curve. For simplicity, we approximated this as 45° off resonance. The motion is measured using the amplitude, R, from the lock-in signal. As the gap changes, the resonant frequency will change, causing the entire curve to shift. Since we are driving at a fixed frequency, the measured R value will also shift.

To determine the driving frequency, we measured a resonance curve, as shown in Figure 5.12.

With the probe positioned ∼680 nm from the anode at a bias of 83 V, we moved the base of the cantilever by applying a 1 Hz sine wave to the piezo. We started with an amplitude of 22 nm and successively decreased it down to 1 nm as seen in Figure 5.13. Below that amplitude, the oscillations were indistinguishable from the noise. There was a large amount of noise in the dc current, most likely from mechanical vibrations in the system. By applying a 10 Hz low pass filter, we can easily see oscillations in the dc current down to an amplitude of 5 nm. This is in agreement with the measured dc sensitivity discussed before. For smaller amplitudes, the oscillations are still visible in the lock-in readout, but not in the dc current.

With a slow drive amplitude of 11 nm, the dc current response measured an amplitude of ∼250 nA and the response in the lock-in amplitude was ∼1 mV. After decreasing the slow drive amplitude to 1.1 nm, the dc response was no longer visible above the noise, but the response in R still had a measurable amplitude of ∼100 µV. At these small displacements, it is easy to see how much the measurements of R are affected when the current jumps by a large amount, as seen at ∼50 s.

For the FM measurement technique, the phase locked loop was set to drive the cantilever on resonance (setting the phase to 0). A measurement of the frequency shows the slow displacement of the base of the cantilever. Again, the probe was positioned ∼650 nm from the anode with a bias of 65 V and the motion was added to the cantilever. The results of this measurement are shown in Figure 5.14. At an oscillation of 11 nm, the dc response was similar to the previous measurement at ∼250 nA. The frequency responded with an amplitude of ∼3 Hz. The dc response was still partially visible at an amplitude of 5 nm, but was lost in the noise for

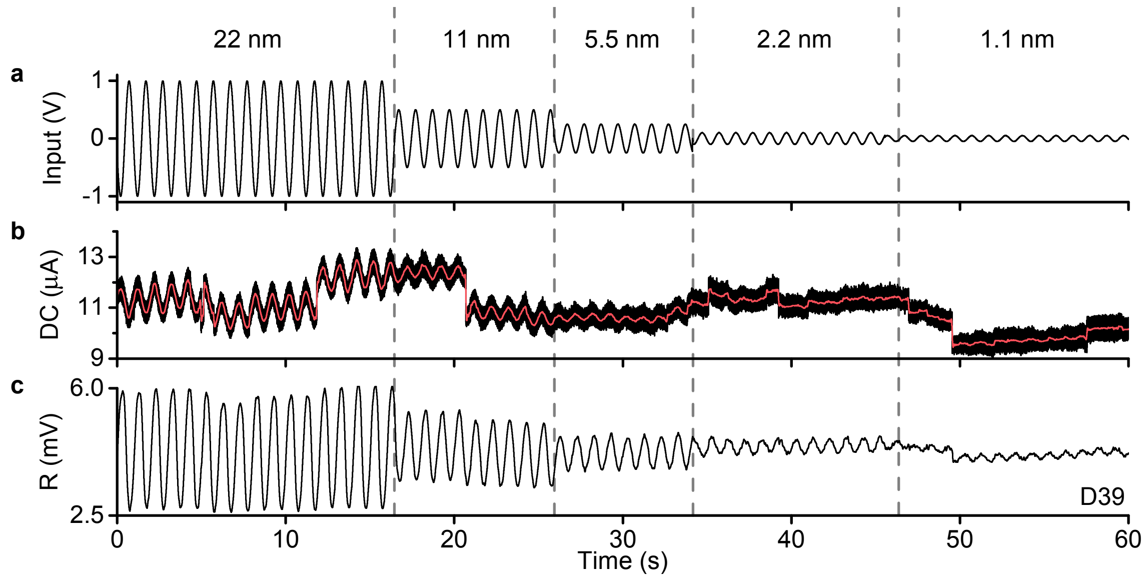

FIGURE 5.13. While driving the probe at a constant frequency (f=199 036 Hz) just off resonance (f_0=199 041 Hz), the base of the cantilever was slowly oscillated while the lock-in readout, R, and the dc current were measured. At an oscillation amplitude of 11 nm, the dc response had an amplitude of 0.24 µA, and the R response had an amplitude of 0.95 mV. At an oscillation amplitude of 1.1 nm, the dc response was not visible above the noise, but the R response was 93 µV. The red curve overlayed on the dc current is the result of applying a 10 Hz low pass filter. The large amount of noise in the dc current is likely due to mechanical vibrations in the vacuum system. For these measurements, the probe was at a gap of $z \sim 680$ nm and the bias voltage was V_{dc}=83 V.

smaller amplitudes. At an amplitude of 550 pm, the frequency response measured an amplitude of 0.14 Hz. The lower noise in this technique allowed us to easily resolve motion down to an amplitude of ∼500 pm. It appears that the frequency measurement is much less sensitive to variations in the current compared to the AM technique. One obvious example is the frequency response when the current spikes at ∼45 s.

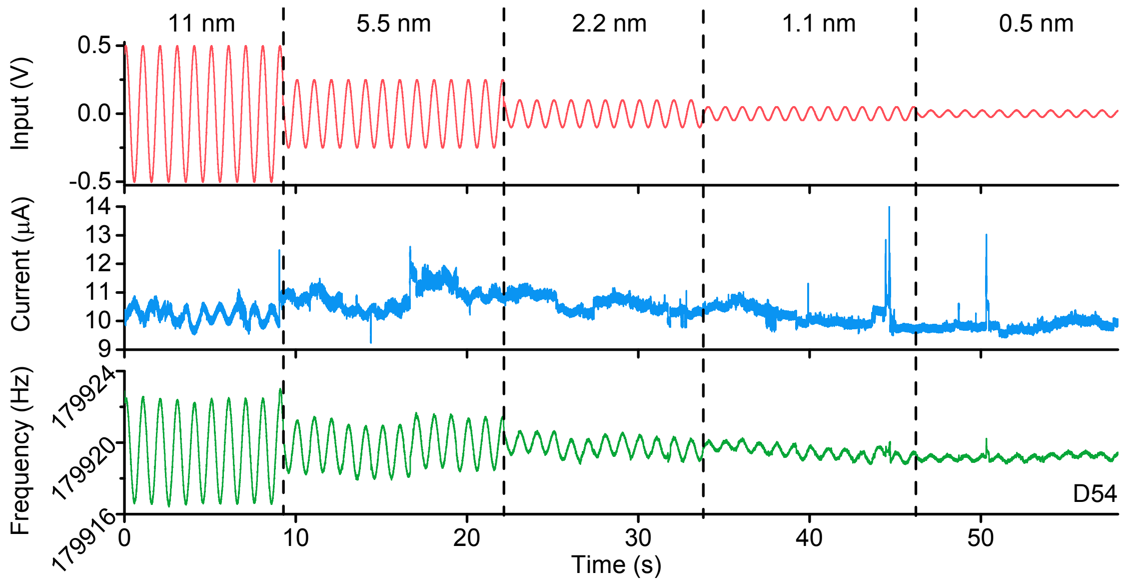

FIGURE 5.14. While driving the probe on resonance using a PLL, the base of the cantilever was slowly oscillated at 1 Hz and the resonance frequency was measured along with the dc current. The probe was located at a gap of z=650 nm, with a bias of V_{dc}=65 V. The amplitude of the cantilever was approximately 17.5 nm based on measurements before probe fabrication. For a slow oscillation with an amplitude of 11 nm, the amplitude of the dc current response was 0.26 µA and the amplitude of the frequency response was 2.88 Hz. With the slow oscillation reduced to an amplitude of 550 pm, the current response was not visible above the level of noise, whereas it is still very clear in the frequency response, which had an amplitude of 0.14 Hz.

5.8. Topographic Measurements

We now test the ability of our nanotube topografiner to image the topography of a surface. To demonstrate imaging, we scan the probe across a periodic metallic structure of bars ((382.5 ± 6.2) nm FWHM, (411.5 ± 3.6) nm FWAB, (50.8 ± 0.2) nm tall, pitch of 2 µm) while simultaneously measuring the frequency at each lateral point $f(z, x)$. An example of one of these bars, measured by AFM, is shown in Figure 5.16. After scanning over the first bar feature at a distance of z=500 nm, we lowered the probe toward the sample by 50 nm and then scan the next bar. We also lowered the bias V_{dc} to match the emission current between scans. The scan results for four distances are shown in Figure 5.15.

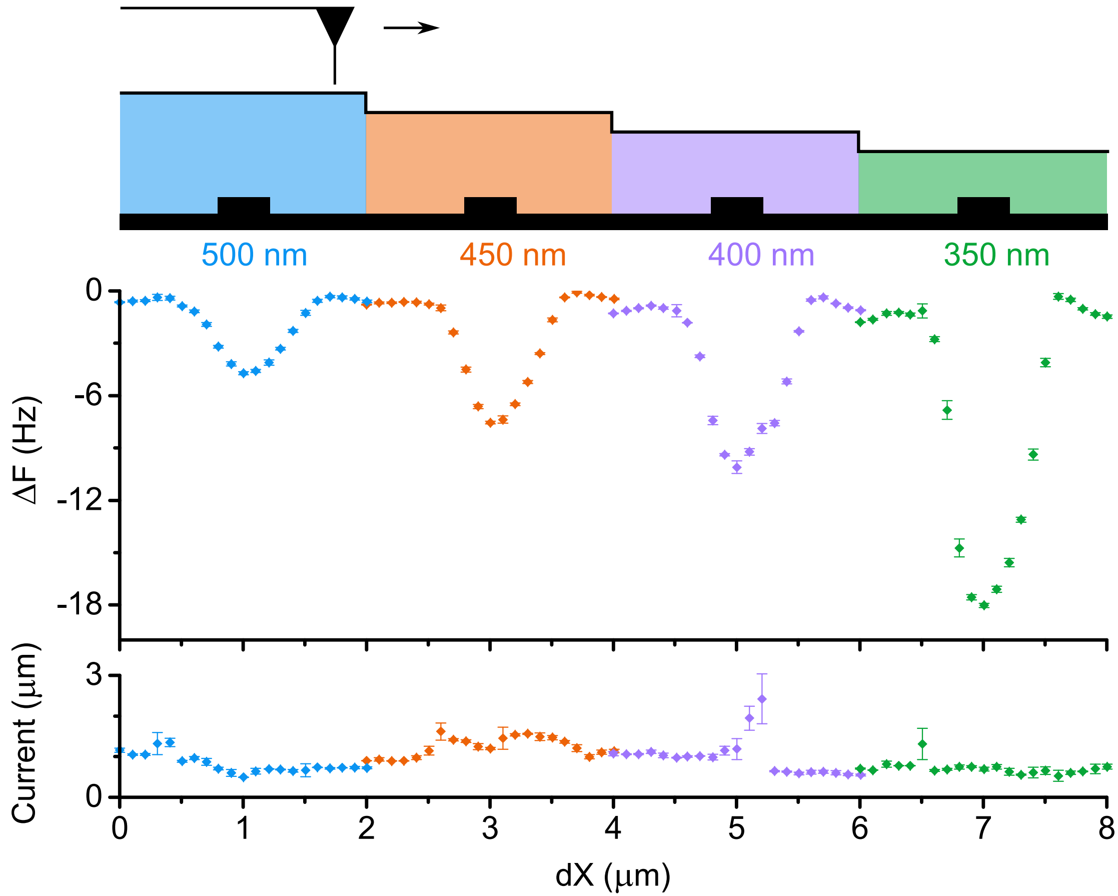

FIGURE 5.15. Measurement of a series of reference bars with the probe. The bars are from the 2 µm pitch area of a Pelcotec CDMS-1T reference sample. They are (50.8 ± 0.2) nm tall with a FWHM of (382.5 ± 6.2) nm. While driving the probe on resonance with a gap of z=500 nm, we scanned the probe across one of the bars. The gap was reduced by 50 nm, and the process repeated. The measured FWHM from these scans was (645 ± 25) nm. The bias for these scans was approximately 40 V, but was decreased between each scan to obtain a field emission current of $\sim$1 µA. As the gap decreased, the magnitude of the frequency change increased by a factor of three. The bars were unable to be resolved using only the dc current.

The relative signal change (Δf) increases in magnitude as the probe is scanned over the feature and is highest over the center of the bar. The Δf is negative due to capacitive softening in the cantilever spring constant. As the probe approached the surface (from 500 nm to 350 nm), the peak Δf value for each bar also increases in magnitude by about a factor of 3. This behavior is expected from the non-linear slope

of $f(z)$ as seen in Figure 5.6, and suggests decreasing z as simple means to boost the imaging signal. By measuring the Δf when changing the gap between bars, we can estimate a calibration $(\partial f/\partial z)$ to correlate a frequency shift from the topographic scan to a height. The calculated heights for each scan are shown in Table 5.1. These heights are close to the actual value of (50.8 ± 0.2) nm as measured by the AFM. The lower part of Figure 5.15 also shows the dc emission current during the scan. At these distances, this current, the principal signal of the original topografiner, does not appear to resolve the bars. By imaging surface features at these values of z, our nanotube topografiner greatly increases the working-distance relative to the original topografiner, as well as modern AFM and STM.

Gap (nm)	Calibration (nm/Hz)	Height (nm)
500	9.06 ± 0.47	42.7 ± 2.4
450	7.63 ± 0.55	57.6 ± 4.2
400	5.68 ± 0.32	57.4 ± 3.8
350	3.37 ± 0.15	60.7 ± 2.8

TABLE 5.1. Table of calibrations for frequency to height conversions in topographic scans. The calibrations are calculated by measuring the frequency shift when the probe is moved by 50 nm. This calibration is combined with the peak frequency shift in Figure 5.15 to determine the height of the bar when measured by the probe. When measured by AFM, the bars were (50.8 ± 0.2) nm tall.

The spatial resolution is broadened primarily by the probe-sample capacitance. The average full width half maximum (FWHM) of the imaged features provides a measure for the lateral spatial resolution. From the data in Figure 5.15, we obtain FWHM=(645 ± 25) nm, giving a dilation of 262 nm relative to the (383 ± 6) nm width of the feature. From this, we estimate the spatial resolution for these scan parameters to be δ=131 nm. Further discussion of the origins of the dilation is found in the next chapter. At 500 nm, the resulting scan is fit very well by a gaussian, but

as the probe descended, the fit became progressively worse. Hopefully this is another indication that the probe is starting to resolve the actual shape of the bar as it gets closer.

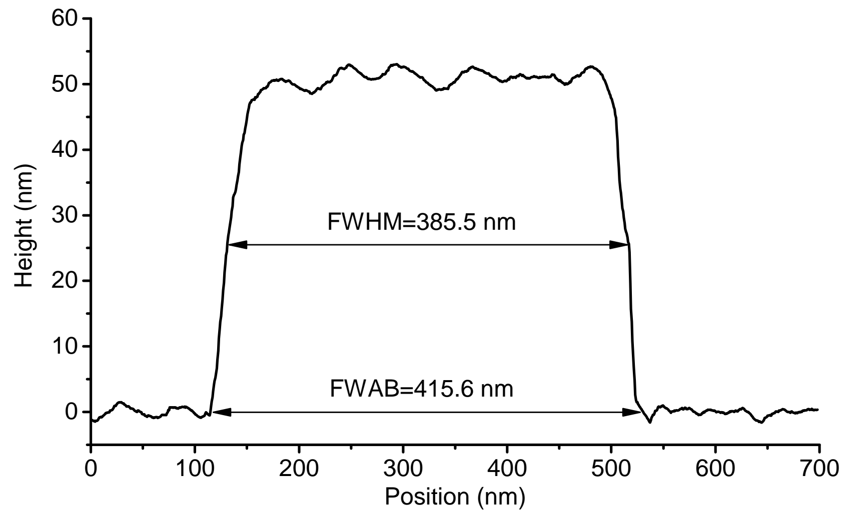

FIGURE 5.16. An example of the cross section of a reference bar measured by AFM. On average, the bars are (50.8 ± 0.2) nm tall, have a FWHM of (382.5 ± 6.2) nm, and are (411.5 ± 3.6) nm wide at the base. The bars have a pitch of 2 µm. These features are located on a Pelcotec CDMS-1T Calibration Standard.

CHAPTER VI

THEORY AND SIMULATIONS

Of the three techniques discussed in the previous chapter, the FM technique was by far the most sensitive. In order to further improve this sensitivity and understand our results, I develop a physical model for our electromechanical system in analytical form. The analytical model consists of electromechanical softening due to capacitive coupling. Through finite element simulations, I determine the capacitance of our high aspect ratio probes to create a model for the frequency shifts, and then apply it to the transverse resolution of the probes. The high aspect ratio nanotube causes large frequency shifts at small distances due to the local interactions with the sample. The small size of the probe should also lead to higher resolution in transverse scanning applications.

6.1. Derivation of Capacitive Spring Constant

The potential energy of a capacitor is given by

$$U(z) = \frac{1}{2}C(z)V^2 \tag{6.1}$$

The capacitor in this case is formed by the probe and anode. We can find the electrostatic force between the anode and the probe using

$$F_C(z) = -\frac{\partial U}{\partial z} = -\frac{1}{2}V^2\frac{\partial C}{\partial z} - CV\frac{\partial V}{\partial z} \tag{6.2}$$

Assuming the voltage is constant with the position, we can Taylor expand about z_0 to get

$$F_C = F_0 + \left(-\frac{1}{2}V^2\frac{\partial^2 C}{\partial z^2}\right)(z - z_0) \tag{6.3}$$

where z_0 is the gap between the anode and the tip of the nanotube and F_0 is the constant force term.

The spring constant of the cantilever, k_0, is defined as

$$F_S = -k_0\delta \tag{6.4}$$

where F_S is the responding force for a displacement of δ. It is easily worked out that $z \propto -\delta$, so the spring constant associated with a spatially varying capacitance is

$$k_C = -\frac{1}{2}V^2\frac{\partial^2 C}{\partial z^2}\bigg|_{z=z_0} \tag{6.5}$$

6.2. Capacitance Simulations

We used COMSOL to perform finite element simulations to determine the capacitance of our probe as a function of the gap between the CNT tip and the anode. The probe is separated into three components: the CNT, the cone of the AFM probe, and the cantilever. The cantilever is modeled as a rectangular prism. The AFM tip is modeled as a cone, set back from the free end of the cantilever. The CNT is modeled as a solid cylinder with a hemispherical cap. The anode is modeled as a large square (to avoid edge effects) covering the bottom of the simulation volume. The simulation volume is extended above the cantilever so that fringing fields are taken into account in the capacitance. These can contribute half of the capacitance for a shape like a cantilever[40]. For the simulation, each component was assigned

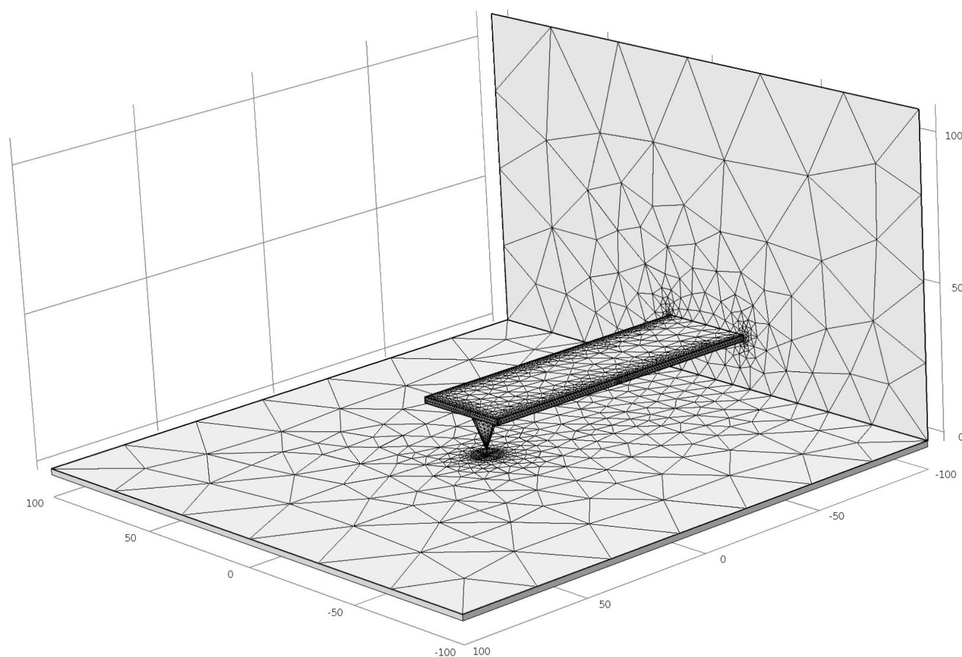

FIGURE 6.1. The geometry and mesh for the finite element simulation of the probe capacitance. The cantilever is 110 µm long by 35 µm wide and 2 µm thick. The cone of the AFM tip is 15 µm tall with a half angle of 20°. The length of the CNT ranged from 1-10 µm, with a radius of 5 nm. The simulation volume is 200 µm square and 100 µm tall. The finest mesh was on the CNT, with a minimum element size of 4 nm.

to be a "Terminal" in COMSOL. This allowed us to extract the capacitance for each component separately.

For the simulation, the cantilever was 110 µm long by 35 µm wide. The tip was 15 µm tall with a half angle of 20°. The simulation volume was 200 µm square and ∼100 µm tall. The height varied depending on the CNT and gap parameters used. We ran simulations for CNTs with a radius of 5 nm and lengths of 1, 2, 5 and 10 µm. The gap between the CNT tip and anode ranged from 100 nm to 5 µm.

For the carbon nanotubes, the simulated capacitance ranged from 10 to 60 aF depending on the length of the nanotube, as shown in Figure 6.2. The capacitance decreased as the gap increased by ∼20% for the longest CNT, and by ∼50% for the shortest. The curvature of the capacitance was highest for $z<1$ µm, so we used a

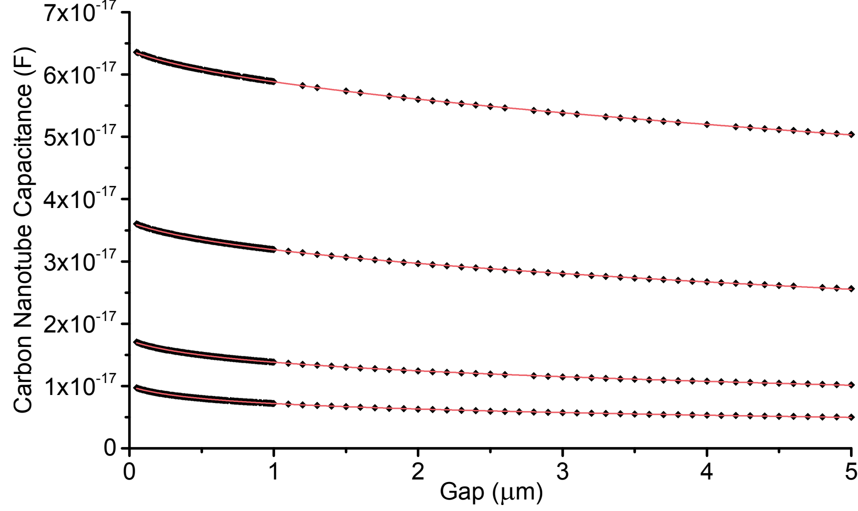

FIGURE 6.2. Results from the finite element simulation showing the capacitance of CNTs of length 1, 2, 5 and 10 µm (bottom to top). Over this range of lengths, the capacitance varies from 10 to 60 aF. Each CNT length is fit using Equation 6.6. The capacitance undergoes the most rapid change for $z < 1\,\mu\text{m}$, so the simulation was ran every 20 nm, then every 100 nm afterwards. The precision in the small z part of the simulation is crucial because the curvature of the capacitance function directly affects the frequency shifts.

smaller step size to increase precision. We fit the capacitance for each part using:

$$C(z) = \frac{A + Bz}{1 + Cz + Dz^2} \tag{6.6}$$

which then gave us a differentiable function to use when finding the capacitive spring constant.

Starting from $f=(1/2\pi)\sqrt{k/m}$, where $k=k_0 + k_C$, we can derive an expression for the new resonance frequency after capacitive softening. This is given by:

$$f = f_0 \left(1 + \frac{k_C}{2k_0}\right) \tag{6.7}$$

where f_0 is the unbiased resonance frequency of the AFM cantilever. Because k_C is negative, it is easy to see that the new frequency will be shifted down relative to the unbiased frequency.

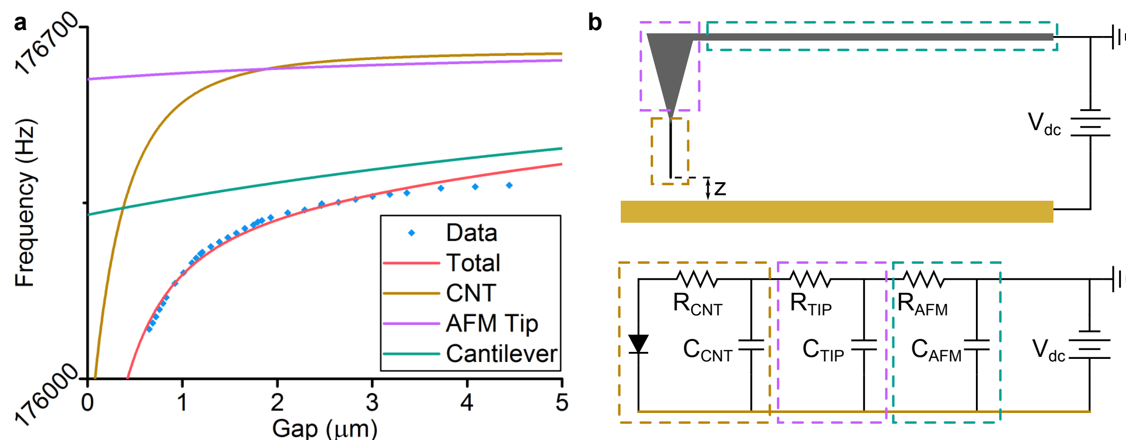

FIGURE 6.3. (a) The frequency data of Probe 21 fitted with the frequency simulation from Equation 6.7, where the fit is the red line. The fitting parameters were k_0=2.49 N/m and f_0=176 656 Hz. The bias for this probe and simulation was V_{dc}=59 V. The simulation used the capacitance modeled from a probe with a 10 µm long, 5 nm radius CNT. The contribution to the frequency from the CNT, AFM tip, and cantilever are broken out. In this case, the AFM tip (purple) played almost no role and the cantilever (green) added mostly a constant offset. The CNT (dark yellow) had a very large contribution to the change in frequency when the gap was below 1 µm. (b) A schematic of the probe-anode system with the associated circuit diagram. Each component of the probe is outlined with a different color, matching the fit in part (a) and the corresponding portion of the circuit diagram.

We use the simulated $f(z)$ for the total capacitance to fit experimental data using only two free parameters: f_0 and k_0. The results from this analysis for a 10 µm long nanotube are shown in Figure 6.3a, together with measured $f(z)$ data for Probe 21. From the fit for this probe, k_0=2.49 N/m, which is within the specified range for these cantilevers, and f_0=176 656 Hz, which differs slightly (∼0.15%) from the frequency measured in SEM before fabrication. The excellent agreement between the fitted and actual parameter values suggests that our capacitive model captures much of the physics of our system. The model predicts that $f(z)$ is determined by

the AFM cantilever (green curve) at large gaps ($z > 4\,\mu$m) and by the nanotube (dark yellow curve) at small gaps ($z < 2\,\mu$m). From the slope $\partial f/\partial z$, the model points out that the high sensitivity (i.e. low η_{FM}) observed at small z (Figure 5.11) is driven by the nanotube capacitance.

	Area (m^2)	z (m)	Effect on Δf
CNT	10^{-16}	10^{-7} to 10^{-6}	10^{12} (small z) to 10^{8} (large z)
Tip	$8 \cdot 10^{-11}$	10^{-5} to $2 \cdot 10^{-5}$	$8 \cdot 10^{9}$ (short CNT) to $5 \cdot 10^{8}$ (long CNT)
Cantilever	$4 \cdot 10^{-9}$	$2 \cdot 10^{-5}$ to $3 \cdot 10^{-5}$	10^{10} (short CNT) to $5 \cdot 10^{9}$ (long CNT)

TABLE 6.1. Estimating the relative effect of the carbon nanotube, AFM tip, and AFM cantilever on the shift in frequency. The carbon nanotube area is the cross section of a 10 nm diameter tube. The tip area is estimated using the circular projection of a cone (15 µm tall with 20° half angle). The cantilever is 110 µm x 35 µm. A short nanotube is considered to be 1 µm and a long nanotube would be 10 µm

This observation agrees with an analytical model for capacitance of each component (nanotube, tip, cantilever), which predicts $\Delta f(z_i) \propto A_i/z_i^4$, where A_i and z_i are the component area and effective distance from the anode for a given gap, respectively (See Table 6.1). For large z, all z_i are also large, so the frequency shift is dominated by the largest area componentthe cantilevers. For small z, z_{CNT} is several orders of magnitude smaller than z_i for the tip or the cantilever. So despite the relatively small area of the nanotube, the $1/z_{CNT}^4$ term enables the nanotube to generate large values of Δf. Moreover, Δf should be dominated by the tip of the nanotube because it is closest to the surface, so we expect that small area of the tip will enable spatially resolved imaging of the surface, even at large z.

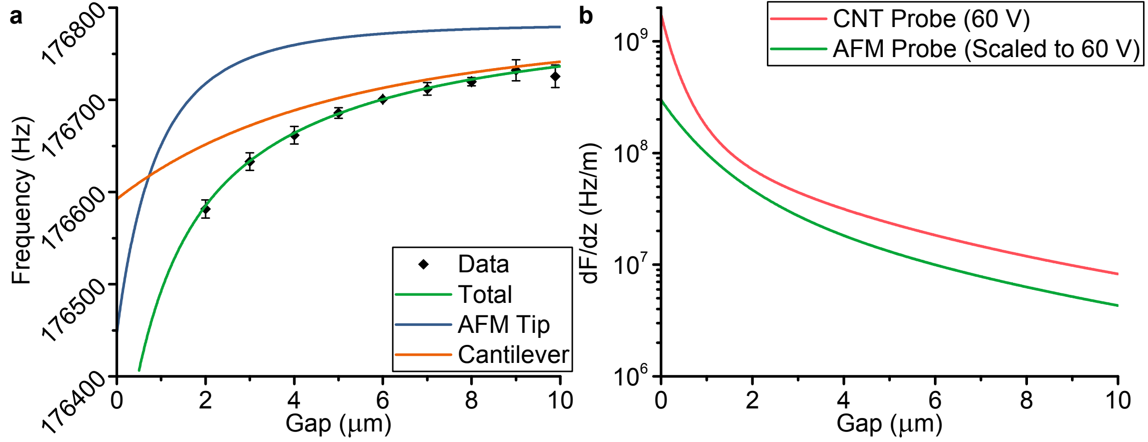

FIGURE 6.4. (a) Fitting the frequency simulation to data taken for a bare AFM probe (no CNT) when biased at 70 V. The fit parameters were $f_0 = 176\,784\,\text{Hz}$ and $k_0 = 26.4\,\text{N/m}$. The blue curve shows the relative frequency shift due to the AFM tip. The orange curve shows the shift due to the cantilever. The green curve represents the total fit. (b) The derivative of the frequency fit gives an idea of the sensitivity of the probe. The carbon nanotube curve is the derivative from Figure 6.3. Scaling the derivative of the bare AFM fit down to 60 V allows us to compare the two. In all cases, the CNT probe has a higher derivative, and should therefore have a better sensitivity. In reality, the AFM probe would get pulled in well before it reached the 100s of nm range at these voltages.

6.3. Bare AFM Tip Measurements

In order to better understand the role that the AFM probe was playing in the capacitance, we measured the frequency shift for a bare AFM probe (with no CNT) that is biased relative to an anode. We also wanted to see if the AFM probe could produce the observed frequency shifts if it was spaced far away from the anode (gap+length CNT). To do this, we used an AFM (Bruker Dimension Icon) and started by extending the piezo to its maximum extent (10 μm). This was required because by default, the piezo is balanced in the middle of its range with 5 μm on each side. Starting with the tip in contact with the anode, we turned off all feedback to keep the AFM probe stationary with respect to the anode. We then retracted the tip by a known amount and measured the resonance frequency while biased and

unbiased. The bias used here was V_{dc}=70 V and the data is shown in Figure 6.4a. When part of a field emission probe, the AFM tip is more than 5 µm away from the anode. At most, the frequency shift when biased would only be 50 Hz, which is much less than the observed 300 Hz shift in Figure 6.3. Even at 2 µm, the frequency shift is only ∼150 Hz, still a factor of two away from the observed shift. For these voltages, a gap of less than 2 µm would greatly increase the chance of pull-in and possible damage to the AFM tip.

We can compare the theoretical sensitivity due to these frequency shifts to the values from a carbon nanotube field emission probe. In order to compare, the fitted curve for the AFM data was scaled to a bias of V_{dc}=60 V, the same as the CNT probe. By looking at the derivative of the frequency shift, we see that the CNT probe always outperforms the AFM probe. Additionally, the AFM probe would reach the point of pull-in well before the CNT probe.

6.4. Broadening in Topographic Scans

To understand the broadening observed in the topographic scans of Section 5.8, we simulated the electrostatic effects on the probe frequency for a nanotube probe near a bar. Because the CNT is the most important component for small gaps, the simulation was reduced from the entire probe to just the CNT for computational simplicity. The nanotube was positioned relative to the bar, starting 1 µm from the center in the transverse direction. We then simulated the capacitance as a function of gap as in the earlier simulations (Figure 6.2). This was repeated for multiple transverse positions, finishing at the center of the bar.

For a nanotube of length 5 µm and bars of 50 nm height and 415 nm width and a gap of z=500 nm, the FWHM of the bar was 612 nm, which is reasonably close

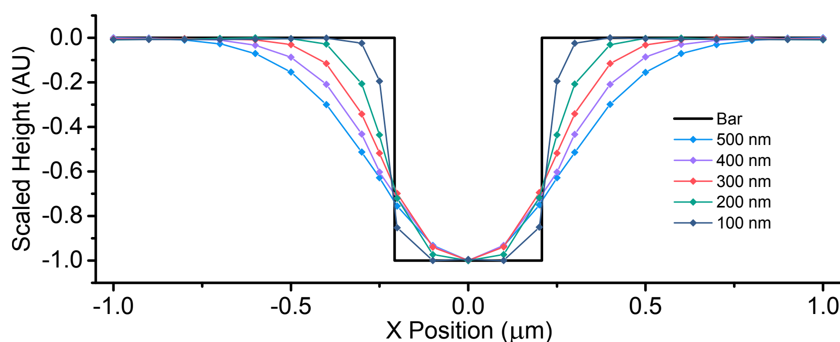

FIGURE 6.5. Simulation of scanning a CNT probe over a rectangular bar 415 nm wide and 50 nm tall. The bar profile is flipped from reality to compare more easily with the simulated results. The measurement from the probe (the frequency shift) will go negative as the probe passes over a protrusion out of the surface. For a gap of 500 nm, the profile is smeared out, and has a FWHM of 612 nm. For a gap of 100 nm, the FWHM is improved to 453 nm. The steps taken in this simulation are 100 nm apart.

to the measured average value of (645 ± 25) nm. Reducing the gap to z=100 nm in the simulation resulted in FWHM=453 nm, suggesting that a reduction in z could improve the spatial resolution. These results are shown in Figure 6.5. The width of the bar for this simulation was chosen based on measurements of the bar width using SEM.

A more accurate model of the bars is based off of the AFM data, which shows the bars have a FWHM of ∼385 nm and are ∼415 nm at the base. This means the bars have a trapezoidal cross section. Repeating the simulation with this cross section gives the results shown in Figure 6.6. At z=100 nm, the FWHM was 379.8 nm and at z=500 nm, the FWHM was 588.8 nm.

A visual interpretation of the broadening can be found by looking at the electric field lines between the probe and anode. The field lines near the nanotube tip are tightly localized, but diverge as they approach the anode surface as shown in Figure 6.7. The spreading of the field lines decreases with smaller gap; for a gap of z=500 nm, the lines spread to a radius of r∼105 nm at the surface, whereas a gap of

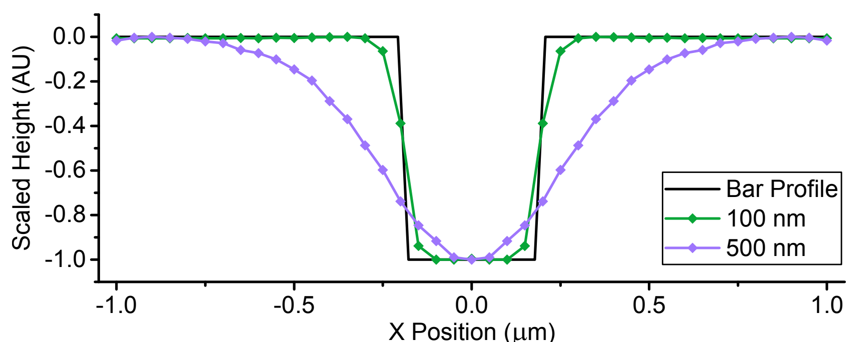

FIGURE 6.6. Simulation of scanning a CNT probe over a 50 nm tall trapezoidal bar with FWHM=385 nm. The base of the bar is 415 nm wide. The bar profile is flipped from reality to compare with the simulated results. The measurement from the probe (essentially the frequency shift) will go negative as the probe passes over a protrusion. For a gap of 500 nm, the profile is smeared out, and has a FWHM of 588.8 nm. For a gap of 100 nm, the FWHM is improved to 379.8 nm. The steps taken in this simulation are 50 nm apart.

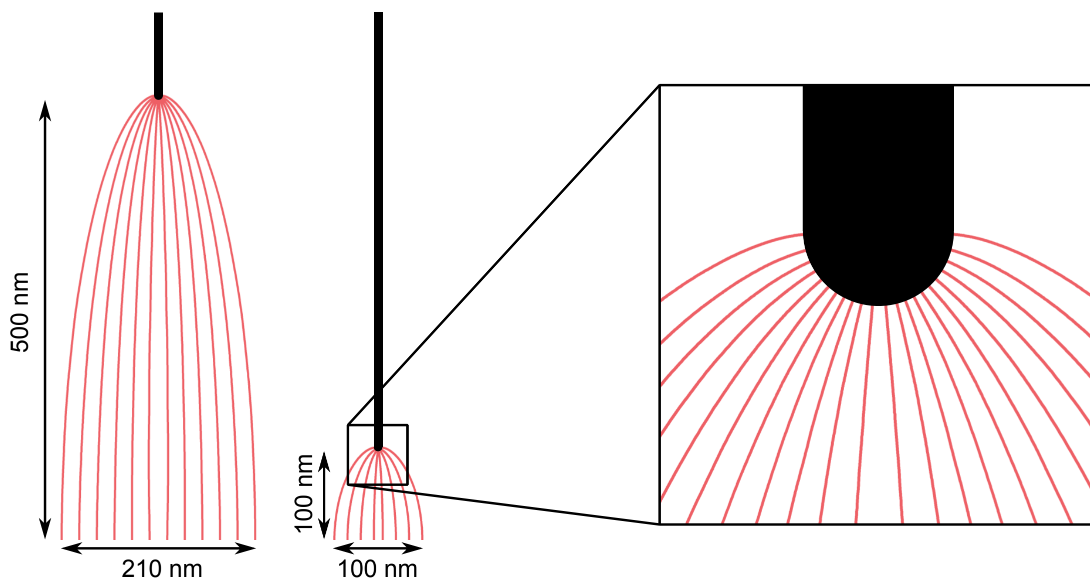

FIGURE 6.7. The electric field lines that originate on the cap of a nanotube spread out as they approach the anode. The CNT here is 5 nm in radius. When the tip of the CNT is 500 nm from the anode, the field lines spread to a radius of 105 nm. When the tip is 100 nm from the anode, the spread is 50 nm in radius. This can be thought of as a simple representation of the amount of anode that the CNT interacts with, forming a capacitor.

z=100 nm yields r∼50 nm. This spread counts all the field lines which originate on the hemispherical cap of the nanotube. Interpreting r as the effective lateral distance over which the nanotube tip interacts with the surface, then the simulated values of r at z=500 nm agree well with the average lateral resolution of our measurements (r=105 nm vs. δ=131 nm) and with the simulated FWHM.

6.4.1. Lateral Deflection

Another broadening effect is expected due to the lateral deflection of the nanotube as it approaches a surface feature. These deflections are a result of transverse electrostatic forces coming from a non planar surface. This effect will cause the nanotube to prematurely interact with those features, thereby dilating their measured width.

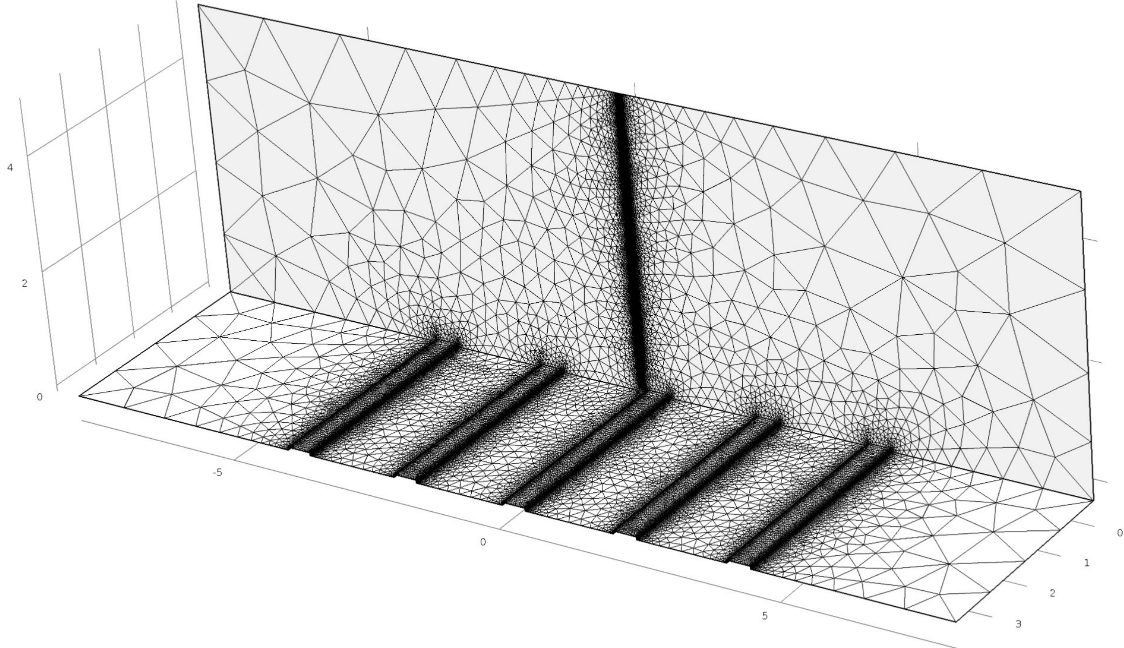

FIGURE 6.8. The geometry for the electromechanical simulations was a series of 5, 500 nm wide by 50 nm tall bars and the position of the CNT was varied from centered between two steps to the center of the middle step. The vertical line of dense mesh is where the CNT is located. The minimum mesh size for this simulation was 4 nm.

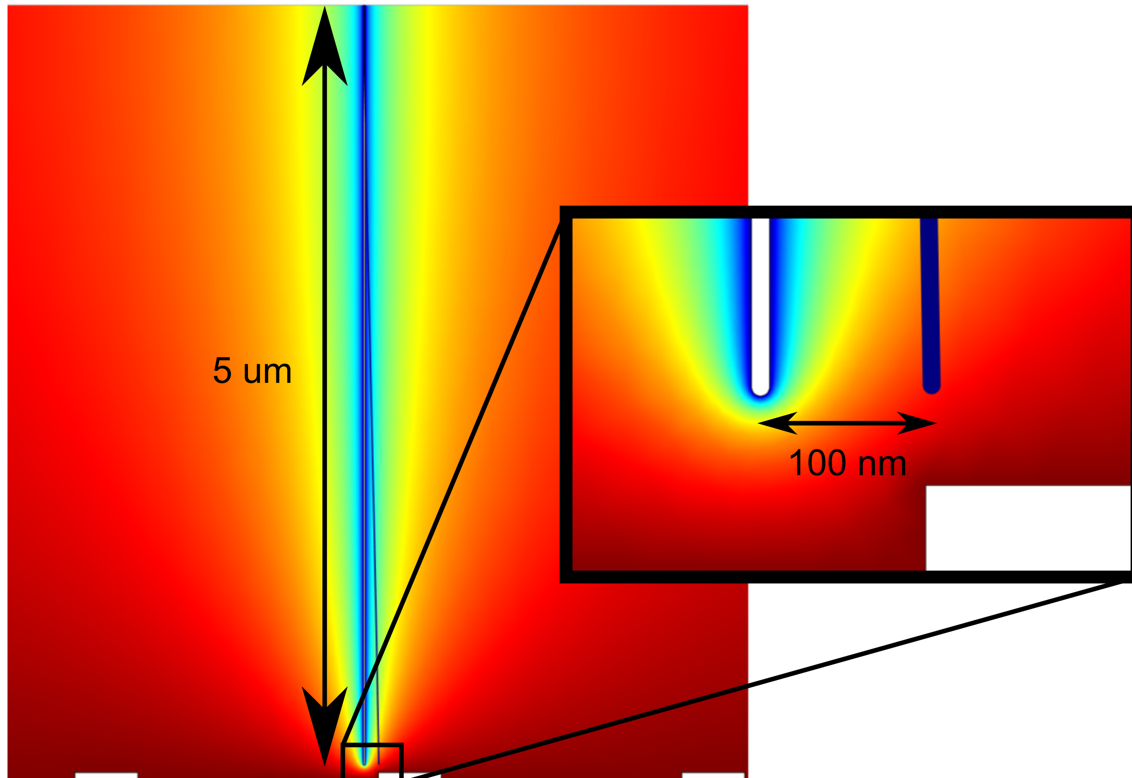

FIGURE 6.9. The potential map from a 3D electrostatic simulation for a 5 µm long and 5 nm radius CNT. Blue represents a voltage of 0 V and the lower boundary was set at a voltage of 10 V. The white rectangle is a cross section of a 500 nm wide by 50 nm tall step. The inset shows the tip of the nanotube was displaced by 100 nm due to the electrostatic forces.

In order to estimate the magnitude of the bending, we created a simulation with a series of 50 nm tall by 500 nm wide steps, spaced by 2 µm, shown in Figure 6.8. When the probe is centered between two steps, the lateral forces from the two closest steps should balance out. Likewise, in the middle of a step, the net force should be zero.

The simulation was split into two phases, an electrostatic phase and a solid mechanics phase. The electrostatic simulation was used to calculate the force on the nanotube. The mechanical simulation applied this force to calculate the bending of

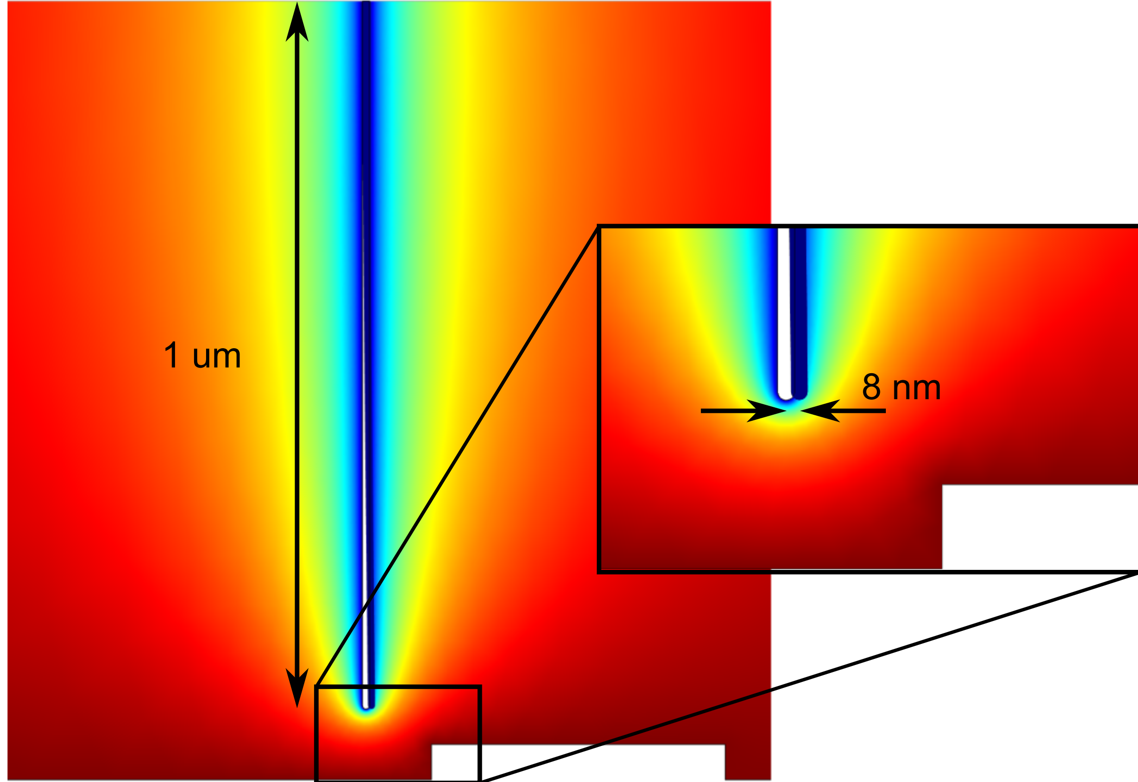

FIGURE 6.10. The potential map from a 3D electrostatic simulation for a 1 µm long and 5 nm radius CNT. Blue represents a voltage of 0 V and the lower boundary was set at a voltage of 10 V. The white rectangle is a cross section of a 500 nm wide by 50 nm tall step. The inset shows the tip of the nanotube was displaced by 8 nm due to the electrostatic forces. At 100 V, the tip of the nanotube is only displaced by 24 nm.

the nanotube. This simplistic simulation will obviously overestimate the amount of bending, but it is a good first order approximation.

We simulated the deflection of a 5 µm nanotube (Figure 6.9), and see bending of order 10 nm at z=500 nm and much larger values of ∼150 nm at z=100 nm (at 100 V bias, 100 nm at 10 V bias). Thus, these deflections are more significant close to the surface, which could counteract the improvements to FWHM discussed above. However, deflections can be mitigated by with a shorter or stiffer nanotube, as shown

for a 1 μm nanotube in Figure 6.10. In this case, the deflection is only of order 10 nm when the tip is close to the surface.

We attempted a full electromechanical simulation, where COMSOL would iterate between electric and mechanical simulations until a steady state was reached. Unfortunately, mesh deformations would tend to cause runaway cases in the simulation. As the nanotube bent, the mesh would be compressed on one side, and expanded on the other. The compressed mesh would then result in larger forces on that side, and would continually compound the problem until an error occurred, usually when the mesh would be compressed so far that it would invert.

CHAPTER VII

CONCLUDING REMARKS

7.1. Summary

In this dissertation, I have shown how a high aspect ratio carbon nanotube field emitter can be used for high precision displacement sensing. I successfully fabricated these probes by attaching a single carbon nanotube to an AFM tip. We can manipulate their position with nanometer precision, make electrical contact, and bias them into field emission.

Combining these field emitters with electromechanical resonant sensing I have greatly enhanced displacement sensing based on field emission. I obtained displacement sensitivities of η=$(7 \pm 4) \cdot 10^2\,\mathrm{fm}/\sqrt{\mathrm{Hz}}$ at a distance of z∼250 nm and a dynamic range (working distance) of several microns. This working distance improves on other SPM techniques by several orders of magnitude.

I used the nanotube Topografiner for two direct applications. The first was as a dynamic micrometer to directly measure displacements of ∼500 pm at a distance of z=650 nm. Additionally, I imaged the topography of a surface with a lateral spatial resolution of ∼100 nm at a working distance of z=500 nm.

I developed a physical model for the electromechanical coupling used for this displacement sensing method. Using finite element simulations I estimated the physical parameters which influence this coupling and applied them to find a close fit to the actual data. These models also show a potential improvement in the lateral resolution by decreasing the working distance, and should be able to resolve topography faithfully even at twice the height of the features being measured.

I have demonstrated that high-aspect-ratio field emitters, such as carbon nanotubes, vastly improve the displacement sensitivity, working distance, and spatial resolution of the topografiner, improvements that are due to the nanometer-scale lateral dimensions of the emitter tip. In terms of the sensitivity, this approach outperforms the original Topografiner by nearly four orders of magnitude, and is competitive with modern AFM and STM.

Measurements of distance will always be important to science and humanity as a whole. Distance, along with time and mass, compose three of the fundamental units of measure in our universe. By improving our ability to measure these quantities, we will continue to push the boundaries on our understanding of the physical world.

7.2. Future Work

In general, these probes could be applied to any sensor with a moving mechanical element that would benefit from a large dynamic range. This could include position sensors, pressure sensors, strain gauges, or accelerometers. The nanotube topografiner could also be used for non-contact scanning probe microscopy, reducing the chances of tip crashing and possibly lead to increases in scanning speed.

These probes could also be used to measure and map large amplitude driven mechanical motion (as opposed to only thermal motion) of nanomechanical resonators with sub-atomic displacement resolution and sub-wavelength lateral resolution. The long working distance could enable a novel means to image sub-surface metallic and conductive structures. This could include electrodes and defects in semiconductor devices buried under several microns of oxide or dielectric materials.

APPENDIX A

FABRICATION DETAILS

A.1. AFM/CNT device fabrication:

1. Deposit carbon nanotubes on substrate
2. Cleave substrate
3. Attach AFM chip to nanopositioners
4. Find CNTs on substrate
5. Touch CNT with AFM tip
6. Deposit platinum to attach CNT
7. Pull CNT off substrate

A.2. On-chip device fabrication:

1. Fabricate large electrodes/bonding pads
2. Spin cast carbon nanotubes
3. Locate carbon nanotubes with SEM (High resolution images)
4. Draw small electrodes in DesignCAD
5. Pattern small electrodes with e-beam lithography
6. Separate devices
7. Release the nanotubes
8. Package device

A.3. Fabrication Techniques

A.3.1. Carbon Nanotube Solution

1. Clean 4 mL vial
2. Take two or three threads of CNT bundles from UCB and place them in vial
3. Crush threads using tweezers
4. Fill vial with IPA
5. Seal cap with parafilm
6. Hold vial in sonicator using clamps
7. Sonicate for 4-5 minutes
8. Invert vial and shake every minute to resuspend threads

A.3.2. Drop casting carbon nanotubes

1. Place substrate on hot plate at 50 °C
2. Use clean glass pipette with rubber bulb to extract CNT solution
3. Place one drop of solution on substrate
4. Wait for solvent to evaporate

A.3.3. Spin casting carbon nanotubes

1. Place substrate on spin coater
2. Use clean glass pipette with rubber bulb to extract CNT-IPA solution
3. Place one drop of solution on substrate
4. Spin substrate at 1000 rpm for 60 s to slowly dry solvent and leave concentric rings of nanotubes
5. Spin substrate at 6000 rpm for 30 s to remove remaining solvent

APPENDIX B

CARE AND FEEDING OF VACUUM CHAMBER

B.1. General Notes

A very complete discussion of real world vacuum system techniques can be found by reading the "Vacuum Lab" chapters. This is located in the "Books" folder on the Alemán Lab server.

B.1.1. Base Pressure

The base pressure of the vacuum chamber ($3 \cdot 10^{-8}$ mbar) is currently limited by the presence of elastomer (viton o-rings for KF) seals in the system. At UHV pressures, air can permeate through the elastomer, giving a constant gas load for the pumps to deal with.

B.1.2. Material Considerations

The platform was fabricated out of brass, which is not ideal for UHV due to the zinc content, but this is mostly a concern at higher than room temperatures. The ideal would have been stainless steel, but it is more difficult to machine. Aluminum would also have been an option, but at the time of fabrication, sources indicated it could be a poor choice for UHV. Thorlabs for one sells aluminum parts for use in vacuum, but only recommends them down to $1 \cdot 10^{-6}$ mbar. There may be ways to improve this with surface treatments of the aluminum as the bare material has a very low outgassing rate. One theory of the poor performance of untreated aluminum is

that water sticks in the oxide layer. As such, anodized aluminum parts should not be used in UHV, nor should any optics pieces with black coating.

B.2. Components

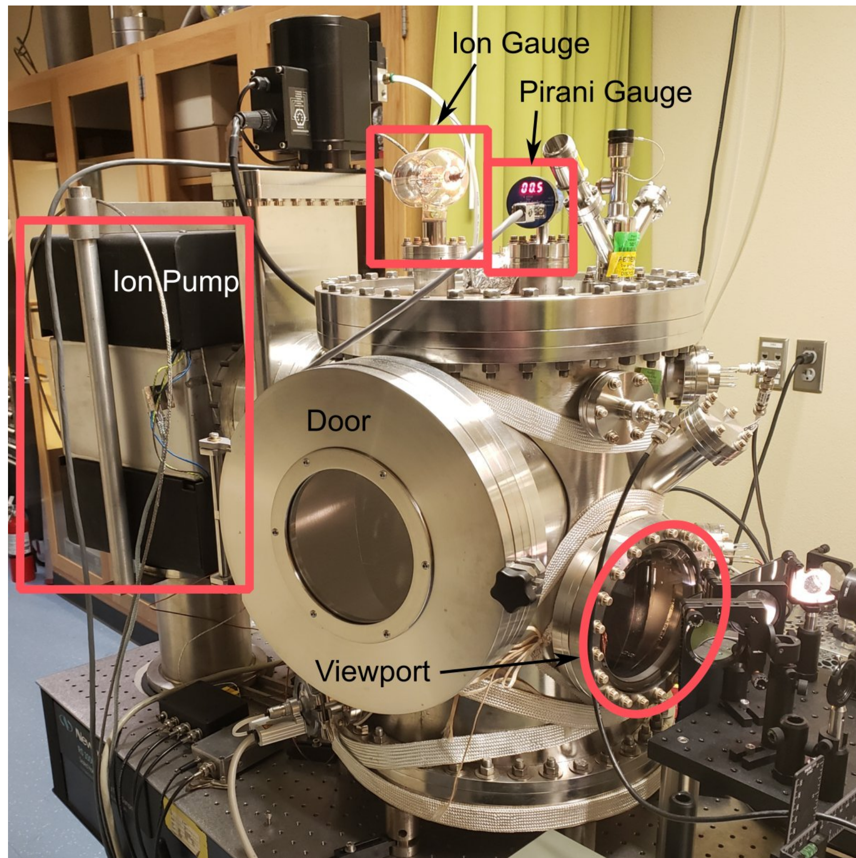

FIGURE B.1. Vacuum System. The measurements for these experiments have to be done in a vacuum environment. The door for sample exchanges is on the near side. The viewport for optical measurements is on the right. The two vacuum gauges are located on top of the chamber. The turbopump is not pictured, but is on the back side of the chamber. The ion pump is located on the left.

B.2.1. Chamber

The vacuum chamber is a stainless steel cylinder with DN350CF (16.5″ CF) flanges on the top and bottom. The cylinder is ∼51 cm tall. On the front is a

DN275CF (13.25″ CF) quick access door with a 15 cm diameter viewport. The door uses an elastomer seal for quickly loading and unloading samples. There is a DN150CF (8″ CF) viewport with a 9 mm thick window on the right side for optical access into the chamber. A DN200CF (10″ CF) pneumatic gate valve is located on the left side and used to seal the ion pump. On the back is a DN63CF (4.5″ CF) elbow and manual gate valve connected to the turbopump. There is a DN100CF (6″ CF) flange currently blocked by the turbopump also on the back. There are 10 DN35CF (2.75″ CF) flanges arrayed around the remainder of the chamber sidewall. These are occupied by the following:

- K-type thermocouple feedthrough
- KF40 adapter
- Isolated BNC feedthrough
- Two 8-pin feedthroughs
- 600 µm fiber optic feedthrough
- Nitrogen feedthrough with manual valve for venting
- Three blank flanges

On top are 2 DN35CF and 1 DN63CF flanges along with the helium flow cryostat (which is also connected with a DN35CF flange). The two smaller flanges are occupied by an ion gauge and a pirani gauge. The larger flange has a D-sub 50 pin feedthrough.

B.2.2. Heating Elements

There are three main heating straps wrapped around the chamber for baking the chamber. There is a separate, smaller heating strap which is wrapped around the main viewport. This smaller strap only needs to be used when baking to extremely

high temperatures to keep the viewport glass from cracking. There are two heating panels mounted underneath the magnets of the ion pump on the top and bottom.

The straps are all connected to a power strip, located on the optical table under the ion pump. The power strip and the ion pump heaters are plugged into a variac, located in the vacuum cabinet. The variac is set to limit the temperature of the chamber to ∼100 °C. The temperature of the system is monitored by three thermocouples. One is inside the chamber, connected to the optical breadboard. Another is underneath the upper magnet of the ion pump. The third is attached to the outside of the chamber wall, above the door.

B.2.3. Pumps

The initial pump down of the chamber is performed by a Varian V70 turbo pump backed by a Varian SD-40 oil sealed rotary vane pump. The turbo pump has a DN63CF inlet/throat and is connected to the chamber through a DN63CF gate valve (Thermionics G-2500-H). This gate valve is manually operated and has a copper gasket on the bonnet flange (where the screw is) and an elastomer gasket on the gate. Once the ion pump is started and reached base pressure, this gate valve is closed and the turbo pump is turned off. Both the turbo pump and roughing pump are controlled by the Varian Turbo-V 70 controller. The turbo pump has a thermocouple gauge to monitor the backing pressure with the readout on the pumping station.

The ion pump is a Varian VacIon Plus 300 controlled by a Varian MidiVac ion pump controller. The ion pump is connected to the chamber by a DN200CF pneumatic gate valve. The gate valve is controlled by a small switch box wired by the previous owners of the vacuum system (Raymer Lab).

From atmospheric pressure to 10^{-4} mbar, the chamber pressure is measured by a Kurt Lesker 275i convection enhanced pirani gauge. This gauge has a breakout box for switching the power and sending the pressure measurement to the computer through the DAQ. Below 10^{-4} mbar, the pressure is measured by a glass tube Bayard-Alpert hot cathode ion gauge. The ion gauge is controlled by a Varian senTorr BA gauge controller.

There is a small manual bellows valve with an elastomer face seal located next to the ion pump for filling the chamber with nitrogen while venting to atmospheric pressure.

B.2.4. Chamber Interior

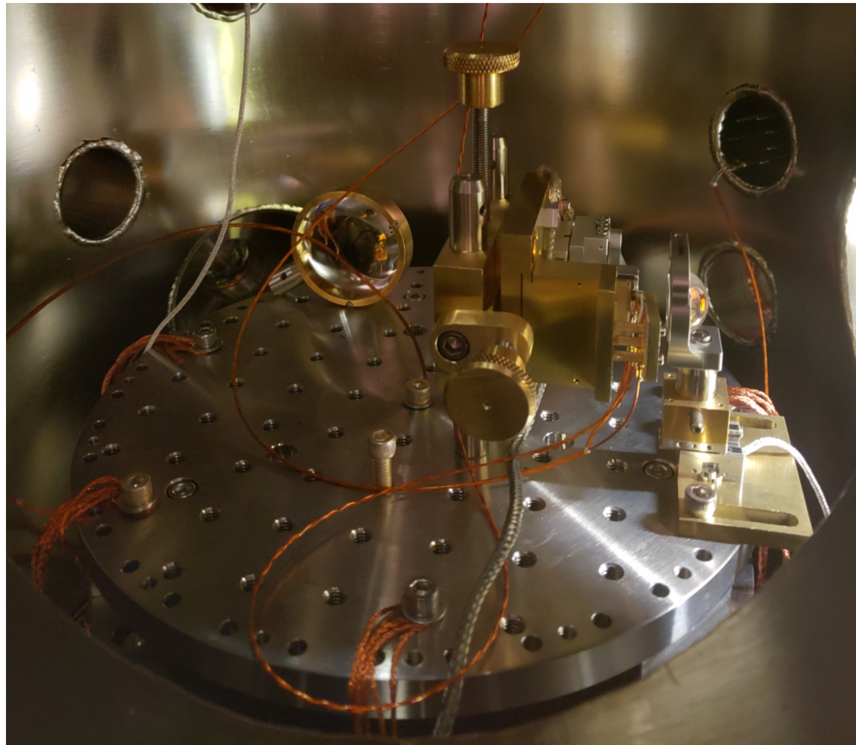

FIGURE B.2. Inside the vacuum chamber is a 10" diameter optical breadboard to mount the objective lens and the piezo platform.

Inside of the chamber is a 10” diameter circular optical breadboard with a 1” grid of 1/4”-20 holes. The breadboard rests on top of an invar disk and three invar blocks from a previous experiment.

A dovetail adapter for the piezo platform is mounted on the breadboard. It has some coarse vertical adjustment (1/4”-28 threaded rod) and coarse horizontal adjustment to push the platform along the dovetail. A separate piezo to control the position of the objective lens is also mounted on the breadboard.

The breadboard is thermally connected to the bottom of the chamber with several copper braids.

B.3. Labview Control/Monitor

There is a labview VI for partially controlling and monitoring the vacuum system called `vacuum_control.vi`. To start a new pumpdown run, set the “`Path`” for data storage, press the “`New?`” button, press the “`Pump Down`” button, then start the VI. With the “`New?`” button pressed, the program will automatically start a new timestamped log file in that “`Path`,” as shown in the “`Save`” box at the bottom. If the “`New?`” button is not pressed, it assumes you are resuming from a previous file and will open a dialogue box for you to find that previous file. With the “`Pump Down`” button pressed, the ion gauge will automatically light when the pressure reaches ~0.01 mbar. When that happens, the “`Emission OFF`” button will turn green and change to “`Emission ON`.” Pressing the button when it is green will turn the ion gauge off, and pressing it when it is grey will turn it on.

To bake the system, press the “`Bake`” button and set the “`Bake Threshold`” temperature. That threshold applies to the internal temperature of the chamber, measured by a thermocouple on the optical breadboard. The “`Bake`” button turns

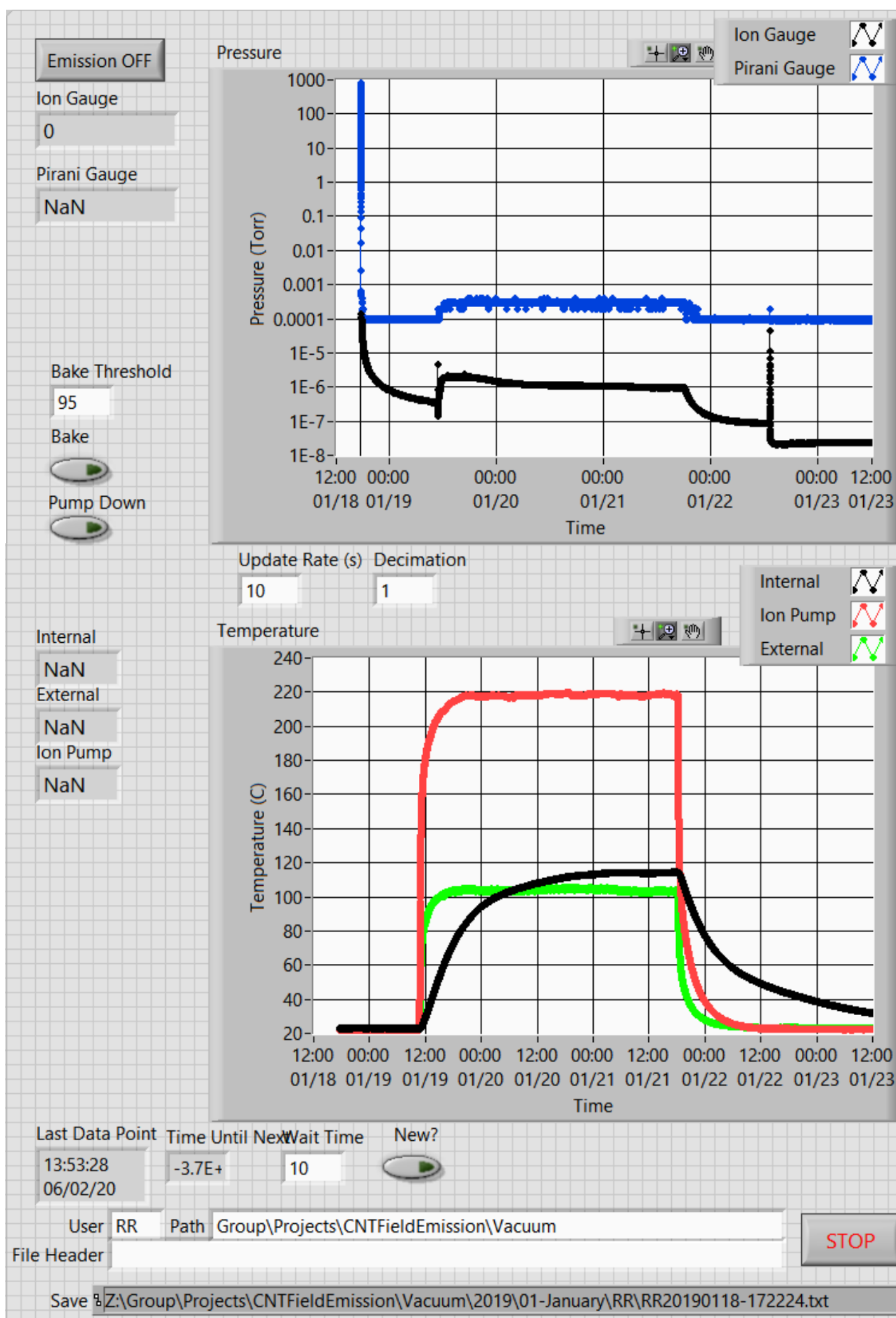

FIGURE B.3. Labview VI for Vacuum Control and Monitoring

on a solid state relay (SSR) in the vacuum cabinet which controls all of the heating elements (discussed above).

You can choose the "`Update Rate (s)`" to change how often the plots are redrawn. If the program has been running for a long time, plotting all of the data can be very resource intensive, so you can choose a value for "`Decimation`" which reduces the plotted data by that factor. This does not change the data written to the log file. The "`Wait Time`" value at the bottom controls the time between data points. The boxes on the left shown the most recent pressure or temperature reading from the vacuum system.

B.3.1. Future Improvements

This VI would benefit from some error catching, for instance if the vacuum pumps cut out and the pressure gets too high, the ion gauge will turn itself off. At that point, when the VI asks for the pressure reading it encounters an error and stops running.

Adding in code to communicate with the ion pump would be a good idea. This would allow for measuring the pressure without the ion gauge and controlling the ion pump remotely.

B.4. Venting Procedure

1. Close gate valve to ion pump
2. Turn off ion pump
3. Start flow of nitrogen
4. Open vent valve to chamber
5. Loosen clamp on door

6. Wait until the chamber reaches atmospheric pressure

B.5. Pump Down Procedure

1. Close the door most of the way
2. Turn off nitrogen
3. Seal door
4. Open turbopump gate valve
5. Start turbopump station
6. Start baking sequence
7. When pressure reaches 10^{-7} mbar, open ion pump gate valve
8. Start ion pump
9. Close turbopump gate valve
10. Turn off turbopump station
11. Let turbopump spin down ($\sim$20 min)
12. Vent turbopump to atmosphere by opening a KF16 seal on the backing side

REFERENCES CITED

[1] A. A. Michelson. Measurement of the Velocity of Light Between Mount Wilson and Mount San Antonio. *The Astrophysical Journal*, 65, 1927.

[2] C. L. Garner. A Geodetic Measurement of Unusually High Accuracy. *Coast and Geodetic Survey Journal*, (April):68–74, 1949.

[3] Albert Einstein. Die Grundlage der allgemeinen Relativitätstheorie. *Annalen der Physik*, 354(7):769–822, 1916. ISSN 00033804. doi: 10.1002/andp.19163540702. URL `http://doi.wiley.com/10.1002/andp.19163540702`.

[4] B. P. Abbott et al. Observation of Gravitational Waves from a Binary Black Hole Merger. *Physical Review Letters*, 116(6):061102, 2 2016. ISSN 0031-9007. doi: 10.1103/PhysRevLett.116.061102. URL `https://link.aps.org/doi/10.1103/PhysRevLett.116.061102`.

[5] G. Binnig, H. Rohrer, Ch. Gerber, and E. Weibel. Surface Studies by Scanning Tunneling Microscopy. *Physical Review Letters*, 49(1):57–61, 7 1982. ISSN 0031-9007. doi: 10.1103/PhysRevLett.49.57. URL `https://link.aps.org/doi/10.1103/PhysRevLett.49.57`.

[6] G. Binnig, H. Rohrer, Ch Gerber, and E. Weibel. Tunneling through a controllable vacuum gap. *Applied Physics Letters*, 40(2):178–180, 1982. ISSN 00036951. doi: 10.1063/1.92999.

[7] G. Binnig, H. Rohrer, Ch. Gerber, and E. Weibel. 7 x 7 Reconstruction on Si(111) Resolved in Real Space. *Physical Review Letters*, 50(2):120–123, 1 1983. ISSN 0031-9007. doi: 10.1103/PhysRevLett.50.120. URL `https://link.aps.org/doi/10.1103/PhysRevLett.50.120`.

[8] G Binnig, C. F. Quate, and Ch. Gerber. Atomic Force Microscope. *Physical Review Letters*, 56(9):930–933, 3 1986. ISSN 0031-9007. doi: 10.1103/PhysRevLett.56.930. URL `https://link.aps.org/doi/10.1103/PhysRevLett.56.930`.

[9] D. Rugar, H. J. Mamin, and P. Guethner. Improved fiber-optic interferometer for atomic force microscopy. *Applied Physics Letters*, 55(25):2588–2590, 1989. ISSN 00036951. doi: 10.1063/1.101987.

[10] Constant A J Putman, Bart G. De Grooth, Niek F. Van Hulst, and Jan Greve. A detailed analysis of the optical beam deflection technique for use in atomic force microscopy. *Journal of Applied Physics*, 72(1):6–12, 1992. ISSN 00218979. doi: 10.1063/1.352149.

[11] R. D. Young, John Ward, and Fredric Scire. The Topografiner: An instrument for measuring surface microtopography. *Review of Scientific Instruments*, 43 (7):999–1011, 1972. ISSN 00346748. doi: 10.1063/1.1685846.

[12] Russell D. Young. Field emission ultramicrometer. *Review of Scientific Instruments*, 37(3):275–278, 1966. ISSN 00346748. doi: 10.1063/1.1720157.

[13] R. H. Fowler and L Nordheim. Electron Emission in Intense Electric Fields. *Proceedings of the Royal Society of London. Series A*, 119(781):173–181, 1928. ISSN 1364-5021. doi: 10.1098/rspa.1928.0091.

[14] Yun-Hi Lee, Chang-Hoon Choi, Yoon-Taek Jang, Eun-Kyu Kim, Byeong-Kwon Ju, Nam-Ki Min, and Jin-Ho Ahn. Tungsten nanowires and their field electron emission properties. *Applied Physics Letters*, 81(4):745, 2002. ISSN 00036951. doi: 10.1063/1.1490625.

[15] Victor I. Kleshch, Denis A. Bandurin, Anton S. Orekhov, Stephen T. Purcell, and Alexander N. Obraztsov. Edge field emission of large-area single layer graphene. *Applied Surface Science*, 357:1967–1974, 2015. ISSN 01694332. doi: 10.1016/j.apsusc.2015.09.160. URL `http://dx.doi.org/10.1016/j.apsusc.2015.09.160`.

[16] Tomomi Yoshimoto, Kazuki Sato, and Tatsuo Iwata. Field emission from a P-type silicon single emitter sharpened by focused ion beam milling. *Japanese Journal of Applied Physics*, 49(7 PART 1):0702121–0702123, 2010. ISSN 00214922. doi: 10.1143/JJAP.49.070212.

[17] Gopal Singh, Robert Bücker, Gnther Kassier, Miriam Barthelmess, Fengshan Zheng, Vadim Migunov, Maximilian Kruth, Rafal E. Dunin-Borkowski, Stephen T. Purcell, and R. J.Dwayne Miller. Fabrication and characterization of a focused ion beam milled lanthanum hexaboride based cold field electron emitter source. *Applied Physics Letters*, 113(9), 2018. ISSN 00036951. doi: 10.1063/1.5039441. URL `http://dx.doi.org/10.1063/1.5039441`.

[18] A G Rinzler, J H Hafner, P Nikolaev, L Lou, S G Kim, D Tomanek, P Nordlander, D T Colbert, and R E Smalley. Unraveling Nanotubes: Field emission from an atomic wire. *Science*, 269(September):1–4, 1995.

[19] Yahachi Saito and Sashiro Uemura. Field emission from carbon nanotubes and its application to electron sources. *Carbon*, 38(2):169–182, 2000. ISSN 00086223. doi: 10.1016/S0008-6223(99)00139-6.

[20] Sumio Iijima. Helical microtubules of graphitic carbon. *Nature*, 354(354):56–58, 1991.

[21] Eric Pop, David Mann, Qian Wang, Kenneth Goodson, and Hongjie Dai. Thermal conductance of an individual single-wall carbon nanotube above room temperature. *Nano Letters*, 6(1):96–100, 2006. ISSN 15306984. doi: 10.1021/nl052145f.

[22] B. Q. Wei, R. Vajtai, and P. M. Ajayan. Reliability and current carrying capacity of carbon nanotubes. *Applied Physics Letters*, 79(8):1172–1174, 2001. ISSN 00036951. doi: 10.1063/1.1396632.

[23] Hongjie Dai, Ali Javey, Eric Pop, David Mann, Woong Kim, and Yuerui Lu. Electrical Transport Properties and Field Effect Transistors of Carbon Nanotubes. *NANO: Brief Reports and Reviews*, 01(01):1–13, 7 2006. ISSN 1793-2920. doi: 10.1142/S1793292006000070. URL `https://www.worldscientific.com/doi/abs/10.1142/S1793292006000070`.

[24] Eric W. Wong, Paul E. Sheehan, and Charles M. Lieber. Nanobeam mechanics: Elasticity, strength, and toughness of nanorods and nanotubes. *Science*, 277 (5334):1971–1975, 1997. ISSN 00368075. doi: 10.1126/science.277.5334.1971.

[25] Yang Wu, Mingyuan Huang, Feng Wang, X M Henry Huang, Sami Rosenblatt, Limin Huang, Hugen Yan, Stephen P O Brien, James Hone, and Tony F Heinz. Determination of the Young's Modulus Nanotubes. *Nano Letters*, 8 (12):4158–4161, 2008. ISSN 1530-6984. doi: 10.1021/nl801563q.

[26] K. Jensen, J. Weldon, H. Garcia, and Alex K Zettl. Nanotube radio. *Nano Letters*, 7(11):3508–3511, 2007. ISSN 15306984. doi: 10.1021/nl0721113.

[27] K. Jensen, Kwanpyo Kim, and Alex K Zettl. An atomic-resolution nanomechanical mass sensor. *Nature Nanotechnology*, 3(9):533–7, 2008. ISSN 1748-3395. doi: 10.1038/nnano.2008.200. URL `http://www.ncbi.nlm.nih.gov/pubmed/18772913`.

[28] Kevin Jensen. *Introduction to the Physics of Electron Emission*. John Wiley & Sons, Inc., 2018. ISBN 9781119051756. doi: 10.1002/9781119051794.

[29] Robert Gomer. *Field Emission and Field Ionization*. American Institute of Physics, 1993. ISBN 1563961245.

[30] F. Ducastelle, X. Blase, J.-M. Bonard, J.-Ch. Charlier, and P. Petit. Electronic Structure. In A. Loiseau, P. Launois, P. Petit, S. Roche, and JP. Salvetat, editors, *Understanding Carbon Nanotubes*, chapter 4, pages 199–276. Springer, Berlin, Heidelberg, 2006. doi: 10.1007/3-540-37586-4{_}4.

[31] Gerwig E. Vibrans. Vacuum voltage breakdown as a thermal instability of the emitting protrusion. *Journal of Applied Physics*, 35(10):2855–2857, 1964. ISSN 00218979. doi: 10.1063/1.1713118.

[32] C. J. Edgcombe and U. Valdrè. Microscopy and computational modelling to elucidate the enhancement factor for field electron emitters. *Journal of Microscopy*, 203(2):188–194, 2001. ISSN 00222720. doi: 10.1046/j.1365-2818.2001.00890.x.

[33] H. Craig Miller. Change in field intensification factor β of an electrode projection (Whisker) at short gap lengths. *Journal of Applied Physics*, 38(11): 4501–4504, 1967. ISSN 00218979. doi: 10.1063/1.1709157.

[34] King-Fu Hii, R Ryan Vallance, Sumanth B Chikkamaranahalli, M Pinar Menguc, and Apparao M Rao. Characterizing field emission from individual carbon nanotubes at small distances. *Journal of Vacuum Science & Technology B: Microelectronics and Nanometer Structures*, 24(3):1081–1087, 2006. ISSN 10711023. doi: 10.1116/1.2188403. URL `http://scitation.aip.org/content/avs/journal/jvstb/24/3/10.1116/1.2188403`.

[35] S T Purcell, P Vincent, C Journet, and Vu Thien Binh. Hot Nanotubes : Stable Heating of Individual Multiwall Carbon Nanotubes to 2000 K Induced by the Field-Emission Current. *Physical Review Letters*, 88(10), 2002. doi: 10.1103/PhysRevLett.88.105502.

[36] Kenneth A. Dean, Paul von Allmen, and Babu R. Chalamala. Three behavioral states observed in field emission from single-walled carbon nanotubes. *Journal of Vacuum Science and Technology B: Microelectronics and Nanometer Structures*, 17(5):1959, 1999. ISSN 0734211X. doi: 10.1116/1.590856. URL `http://scitation.aip.org/content/avs/journal/jvstb/17/5/10.1116/1.590856`.

[37] James F Hainfeld. Understanding and using field emission sources. Technical report, Brookhaven National Lab, 1977.

[38] David W. Allan. Statistics of Atomic Frequency Standards. *Proceedings of the IEEE*, 54(2):221–230, 1966. ISSN 15582256. doi: 10.1109/PROC.1966.4634.

[39] a.G. Umnov and V.Z. Mordkovich. Field-induced evaporation of carbon nanotubes. *Applied Physics A Materials Science & Processing*, 73:301–304, 2001. ISSN 0947-8396. doi: 10.1007/s003390100906.

[40] S. Chowdhury, M. Ahmadi, and W. C. Miller. A closed-form model for the pull-in voltage of electrostatically actuated cantilever beams. *Journal of Micromechanics and Microengineering*, 15(4):756–763, 2005. ISSN 09601317. doi: 10.1088/0960-1317/15/4/012.